

1 **NONLINEAR BIAS CORRECTION FOR SATELLITE DATA**
2 **ASSIMILATION USING TAYLOR SERIES POLYNOMIALS**

3 Jason A. Otkin*

4 *Department of Mathematics and Statistics, University of Reading, Reading, UK*

5 *Cooperative Institute for Meteorological Satellite Studies, Space Science and Engineering*

6 *Center, University of Wisconsin-Madison, Madison, WI, USA*

7 Roland Potthast

8 *Deutscher Wetterdienst, Offenbach, Germany*

9 *Department of Mathematics and Statistics, University of Reading, Reading, UK*

10 Amos Lawless

11 *Department of Mathematics and Statistics, University of Reading, Reading, UK*

12 *Department of Meteorology, University of Reading, Reading, UK*

13 *Corresponding author address: Jason A. Otkin, 1225 W. Dayton St., Madison, WI 53706.

14 E-mail: jasono@ssec.wisc.edu

ABSTRACT

15 Output from a high-resolution ensemble data assimilation system is used
16 to assess the ability of an innovative nonlinear bias correction (BC) method
17 that uses a Taylor series polynomial expansion of the observation-minus-
18 background departures to remove linear and nonlinear conditional biases from
19 all-sky satellite infrared brightness temperatures. Univariate and multivariate
20 experiments were performed in which the satellite zenith angle and variables
21 sensitive to clouds and water vapor were used as the BC predictors. The re-
22 sults showed that even though the bias of the entire observation departure
23 distribution is equal to zero regardless of the order of the Taylor series expan-
24 sion, there are often large conditional biases that vary as a nonlinear function
25 of the BC predictor. The linear 1st order term had the largest impact on the
26 entire distribution as measured by reductions in variance; however, large con-
27 ditional biases often remained in the distribution when plotted as a function
28 of the predictor. These conditional biases were typically reduced to near zero
29 when the nonlinear 2nd and 3rd order terms were used. The univariate results
30 showed that variables sensitive to the cloud top height are effective BC predic-
31 tors especially when higher order Taylor series terms are used. Comparison
32 of the statistics for clear-sky and cloudy-sky observations revealed that non-
33 linear departures are more important for cloudy-sky observations as signified
34 by the much larger impact of the 2nd and 3rd order terms on the conditional
35 biases. Together, these results indicate that the nonlinear BC method is able
36 to effectively remove the bias from all-sky infrared observation departures.

37 **1. Introduction**

38 The ability to generate accurate cloud and water vapor (WV) analyses suitable for numerical
39 weather prediction (NWP) models is perhaps the most challenging aspect of modern data as-
40 simulation (DA) systems because they typically assume Gaussian error statistics and that linear
41 relationships exist between the observations and model state variables. Cloud processes, however,
42 are inherently nonlinear with complex interactions occurring between different cloud hydrometeor
43 species and the local thermodynamic environment at spatial and temporal scales that are typically
44 much smaller than those represented by NWP models. Likewise, WV content can change rapidly
45 in space and time and can influence the evolution of the cloud field in nonlinear ways. These and
46 other factors can make it very challenging to effectively assimilate information from cloud and
47 WV sensitive observations.

48 Remotely sensed observations obtained using geostationary and polar-orbiting satellites provide
49 the only reliable source of high-resolution cloud and WV information covering large geographic
50 domains. Sophisticated visible, infrared, and microwave sensors onboard various satellite plat-
51 forms provide information about the spatial distribution and characteristics of the cloud and WV
52 fields. For regional-scale NWP, observations from geostationary satellites are especially useful
53 because their continuous viewing of the same area with high temporal and spatial resolution allow
54 them to more easily constrain the evolution of rapidly changing weather features (Vukicevic et al.
55 2006; Errico et al. 2007). Satellite observations, however, often exhibit biases when compared to
56 their model equivalents computed using the NWP model background; therefore, bias correction
57 (BC) methods are typically required to assimilate these observations (Eyre 2016).

58 Observation-minus-background (OMB) biases can occur for a variety of reasons and can differ
59 for clear and cloudy observations. For example, biases can arise from calibration errors in a satel-

60 lite sensor or to instrument "drift" as a sensor ages. Biases can also be introduced by deficiencies
61 in the forward radiative transfer models used to compute the model equivalent brightness temper-
62 atures. For clear-sky observations, biases may result from errors in the specification of surface
63 emissivity, simplifications in the radiative transfer model equations, inadequate vertical resolu-
64 tion or a low model top in the NWP model, or the misspecification or absence of atmospheric
65 constituents (such as aerosols) observed by some satellite bands. In the context of clear-sky DA,
66 biases can also be introduced by incomplete cloud screening procedures that allow some cloud-
67 affected observations to pass quality control and thereby incorrectly enter the DA system. Indeed,
68 most existing quality control methods were originally designed to remove all cloud-affected obser-
69 vations; however, these constraints are being relaxed as operational modeling centers move toward
70 all-sky DA (e.g., Okamoto et al. 2014; Zhu et al. 2016). Exclusion of cloud-affected brightness
71 temperatures has the undesirable consequence of removing observations that could have been used
72 to improve the model initialization in cloudy areas of the model domain.

73 Additional uncertainties regarding the specification of cloud properties arise when assimilating
74 cloud-affected infrared brightness temperatures. Though forward radiative transfer modeling for
75 cloudy scenes has become more accurate in recent years, deficiencies remain, especially for ice
76 clouds. Simulation of absorption and scattering properties for liquid clouds is relatively straight-
77 forward because the droplets are assumed to be spherical. However, there are larger uncertainties
78 with ice cloud bulk optical properties because there is some dependence in the infrared on the
79 shape of the ice particles (Yang et al. 2013). For example, an ice particle may take the form of a
80 hexagonal plate, solid or hollow column, bullet rosette, or an aggregate of some form, and impact
81 the bulk microphysical and optical properties that result from integration of the individual particle
82 properties over the assumed size and habit distributions (Baum et al. 2014). In addition, the ice
83 water path is related to both the cloud optical thickness and the cloud particle effective diameter.

84 When computing simulated brightness temperatures, these diameters should be computed using
85 the particle size distribution and cloud property assumptions made for each cloud species by a
86 given microphysics scheme (e.g. Otkin et al. 2009; Cintineo et al. 2014; Thompson et al. 2016).

87 Biases in the OMB departures can also be caused by systematic errors in the NWP model fore-
88 casts that result from deficiencies in the parameterization schemes or other characteristics of the
89 NWP model. It is well known that model forecasts containing large biases influence the behav-
90 ior of BC methods and can degrade the performance of DA systems (Dee 2005; Dee and Uppala
91 2009; Eyre 2016). Biases can be especially large for model variables for which few observations
92 are available to constrain their evolution, such as root zone soil temperature and moisture (Mahfouf
93 2010), or variables such as clouds and water vapor that are strongly influenced by parameteriza-
94 tion schemes accounting for sub-grid scale processes. For example, uncertainties in microphysical
95 parameters controlling cloud generation and decay processes can lead to systematic errors in the
96 spatial extent, optical thickness, and height of the clouds, which in turn impacts the simulated
97 satellite brightness temperatures (Otkin and Greenwald 2008; Cintineo et al. 2014; Eikenberg et
98 al. 2015). Ideally, a BC method would not remove the bias in the OMB departures associated
99 with deficiencies in the NWP model because the observations should be used to correct such sys-
100 tematic errors. In the absence of a perfect reference analysis, however, it can be very difficult to
101 determine whether a bias originates in the observations or forward radiative transfer model, both
102 of which should be corrected, or in the model background (Dee 2005). Because of this uncertainty
103 in bias attribution, all BC methods functionally act to correct the bias in the "observations" regard-
104 less of the true sources of the bias (Dee and Uppala 2009). Though this outcome is not desirable
105 because it will limit the ability of the observations to reduce systematic errors in the analysis, it
106 does satisfy the requirement by most DA methods that the observations are unbiased. In addition,
107 the bias corrected observations can still be used to reduce random errors in the analysis. Eyre

108 (2016) noted that the impact of model bias on the analysis accuracy depends on the rate at which
109 the NWP model state relaxes back toward its own climatology after the assimilation update. If
110 an NWP model quickly returns to its preferred state, then the analysis errors will continue to be
111 large even if the model bias can be removed prior to computing the BC coefficients. This points
112 toward the need to fix the bias at its source within the NWP model. The impact of model bias on
113 a BC method can be reduced when high quality "anchor" observations with little or no bias are
114 available; however, it is not apparent that such observations exist for water vapor and clouds.

115 BC methods can be broadly categorized into two types (Eyre 2016). The first type uses depart-
116 tures between the observations and their model equivalents accumulated over long time periods
117 outside of the DA system to estimate and remove the bias from the observations prior to their
118 assimilation. These so-called "static" BC methods typically use the satellite scan angle along with
119 several atmospheric variables, such as the geopotential thickness over some layer, as the BC pre-
120 dictors. The BC coefficients for each satellite sensor and band are then computed using linear
121 least squares regressions between the predictors and the observations. In practice, however, these
122 "static" BC coefficients are regularly updated to account for changes in the model background due
123 to changes in the NWP model or DA system, the addition of new observations, and upgrades to
124 the forward radiative transfer model. Frequent retuning of a static BC method can be beneficial
125 because it makes it more adaptable to changes in the models and observations. More detailed de-
126 scriptions of static BC methods can be found in Eyre (1992), Harris and Kelly (2001), and Hilton
127 et al. (2009).

128 With the second type of BC method, known as variational BC (VarBC), the BC coefficients are
129 updated simultaneously with the control vector during each DA cycle using the same set of obser-
130 vations and an augmented control vector (Derber et al. 1991; Parrish and Derber 1992; Derber and
131 Wu 1998; Dee 2005; Auligne et al. 2007; Dee and Uppala 2009; Zhu et al. 2014). Like static BC

132 methods, VarBC typically uses the satellite scan angle and several variables describing the atmo-
133 spheric state as the predictors, with the total BC treated as a linear combination of all predictors.
134 The BC coefficient for each predictor is computed during the minimization of the variational cost
135 function. With an incremental DA approach with multiple outer loops, the BC coefficient incre-
136 ments evolve during each iteration of the inner loop and are updated at the end of each outer loop,
137 which allows the coefficients to adjust with time and capture changes in observation quality. The
138 state space augmentation approach used by VarBC also requires an estimate of the background
139 covariances of the augmented state vector. For simplicity, most schemes assume that the error for
140 a given BC parameter is uncorrelated with errors in other parameters for other satellite sensors and
141 bands and with errors in the model background (Derber and Wu 1998; Dee 2005).

142 Most BC methods have been developed for use in variational or hybrid DA systems; however,
143 several studies have also explored BC in ensemble DA systems. Fertig et al. (2009) developed a
144 BC method for ensemble DA that is similar to VarBC in that it uses state augmentation to estimate
145 the biases during the assimilation step. They showed that their method was able to reduce both the
146 observation bias and the analysis error in perfect model experiments. Similar methods have also
147 been used successfully in real data experiments assimilating microwave brightness temperatures
148 (Szunyogh et al. 2008; Aravequia et al. 2011; Miyoshi et al. 2011). In high-resolution observ-
149 ing system simulation experiments assimilating infrared brightness temperatures, Cintineo et al.
150 (2016) found that the analysis and forecast accuracy was improved when a simple fixed-value BC
151 was applied to the clear-sky observations similar to that used by Stengel et al. (2009, 2013) in
152 a variational DA system. Cintineo et al. (2016), however, did not bias-correct the cloudy obser-
153 vations prior to their assimilation because their bias was too complex to properly handle using a
154 simple fixed-value BC applied uniformly to all cloudy observations. Zhu et al. (2016) handled bi-
155 ases in all-sky microwave observations by computing the BC coefficients using only cases where

156 both the model background and the observations were either clear or cloudy. By doing this, they
157 were able to reduce errors associated with mismatched cloud fields, while still preserving cloud-
158 dependent information in the matched observations. Together, these results provide evidence that
159 more sophisticated BC methods that can account for changes in cloud properties are necessary to
160 effectively remove biases in the OMB departures.

161 In this study, we present a new BC method that can be used to diagnose and remove biases in
162 all-sky infrared brightness temperatures using a Taylor series polynomial expansion of the OMB
163 departures. This approach can diagnose both linear and nonlinear bias components through use
164 of higher order Taylor series terms and a set of BC predictors. For example, with a 3rd order
165 approximation, the 0th and 1st order terms represent the constant and linear bias components,
166 whereas the 2nd (quadratic) and 3rd (cubic) order terms represent nonlinear bias components. We
167 use this nonlinear BC (NBC) method to remove the bias from Scanning Enhanced Visible and
168 Infrared Imager (SEVIRI) infrared brightness temperatures that were passively monitored during
169 high-resolution ensemble DA experiments. The paper is organized as follows. The DA framework
170 is described in Section 2, with a mathematical description of the NBC method presented in Section
171 3. Statistics obtained using the NBC method are shown in Section 4, with conclusions and a
172 discussion presented in Section 5.

173 **2. Experimental Design**

174 *a. SEVIRI Satellite Datasets*

175 The SEVIRI sensor onboard the Meteosat Second Generation satellite provides accurate top-
176 of-atmosphere radiance measurements across 12 visible and infrared spectral bands with a nadir
177 resolution of 3 km for all infrared bands (Schmetz et al. 2002). The utility of the NBC method was

178 evaluated using brightness temperatures from the 6.2 μm and 7.3 μm bands sensitive to WV over
179 broad layers of the upper and middle troposphere, respectively, when skies are clear, while also
180 being sensitive to clouds when they are present. Under clear conditions, the weighting functions
181 that depict how much radiation from a given atmospheric height reaches the top of the atmosphere
182 peak near 350 hPa (500 hPa) for the 6.2 μm (7.3 μm) bands, and then decrease to zero in the
183 lower troposphere. When clouds are present, however, the weighting functions are truncated near
184 the cloud top, which means that a larger portion of the top-of-atmosphere radiation originates at
185 higher (e.g. colder) altitudes than would occur under clear-sky conditions. Their dual sensitivity
186 to clouds and WV means that observations from these bands provide valuable information about
187 the atmospheric state that is typically not available with conventional observations. Another mo-
188 tivation for using these bands is the expectation that their OMB departure statistics will be more
189 Gaussian than would occur with infrared "window" bands because there will be a smoother tran-
190 sition between the brightness temperatures in adjacent clear and cloudy areas.

191 Cloud top height retrievals made using SEVIRI observations were also obtained using software
192 provided by the EUMETSAT Nowcasting Satellite Applications Facility and will be used as one
193 of the BC predictors. The cloud top height for each satellite pixel was estimated by computing
194 simulated clear-sky 10.8 μm brightness temperatures using the RTTOV radiative transfer model
195 (Saunders et al. 1999) and temperature and humidity profiles from the global GME model (Majew-
196 ski et al. 2002), and then inserting a cloud at successively higher levels until a best fit is obtained
197 between the observed and simulated brightness temperatures (Derrien and Le Gleau 2005; Le
198 Gleau 2016). To reduce the data volume and minimize the impact of spatially correlated errors
199 in the observation departures, the cloud top height retrievals and SEVIRI brightness temperatures
200 were horizontally thinned by a factor of 5 in the zonal and meridional directions. This reduces
201 their horizontal resolution to $\sim 20\text{-}25$ km across the model domain, and is ~ 8 times coarser than

202 the NWP model resolution. The cloud top height retrievals have a vertical resolution of 200 m;
203 however, their uncertainty is larger, especially for semi-transparent clouds (Le Gleau 2016).

204 *b. KENDA Data Assimilation System*

205 Ensemble DA experiments in which conventional observations were actively assimilated and
206 SEVIRI brightness temperatures were passively monitored were performed using the Kilometer-
207 scale Ensemble Data Assimilation (KENDA) system (Schraff et al. 2016) developed by the
208 Deutscher Wetterdienst (DWD). The KENDA system is based on the local ensemble transform
209 Kalman filter method described by Hunt et al. (2007) and uses the Consortium for Small-scale
210 Modeling (COSMO) model (Baldauf et al. 2011) as the NWP model. During this study, ra-
211 diosonde, surface, wind profiler, and aircraft observations, were actively assimilated using a 1-h
212 assimilation window, whereas SEVIRI 6.2 μm and 7.3 μm brightness temperatures were passively
213 monitored. With KENDA, 4-D assimilation capabilities are obtained through inclusion of the ob-
214 servation operators within the COSMO model so that the model equivalents can be computed at
215 the exact observation times during the forward integration of the ensemble. Temporally and spa-
216 tially varying covariance inflation values are obtained at each grid point through a combination
217 of multiplicative covariance inflation based on Anderson and Anderson (1999) and the relaxation
218 to prior perturbations approach described by Zhang et al. (2004). Covariance localization is per-
219 formed by updating the analysis at each grid point using only those observations located within
220 a specified distance of the grid point. The vertical localization scale is fixed, but increases with
221 height, whereas the horizontal scale is determined adaptively. For more detailed information about
222 the KENDA system, the reader is referred to Schraff et al. (2016).

223 This study uses output from ensemble DA experiments that were performed on the COSMO-DE
224 domain covering all of Germany and parts of surrounding countries with 2.8 km horizontal grid

225 spacing. Lateral boundary conditions were obtained at hourly intervals from the 7-km resolution
226 COSMO-EU domain run at the DWD, which in turn is driven by boundary conditions provided
227 by the Icosahedral non-hydrostatic (ICON) model (Zangl et al. 2015). The COSMO-DE domain
228 covers approximately 1200 x 1200 km and contains 50 vertical levels that are terrain-following in
229 the lower troposphere and become horizontally flat in the upper troposphere and stratosphere. The
230 model top is located at 22 km (i.e. about 40 hPa). The DA experiments employed 40 ensemble
231 members along with a deterministic run that is initialized by applying the Kalman gain matrix from
232 the assimilation update to the deterministic model background. The ensemble and deterministic
233 runs were initialized at 00 UTC on 16 May 2014 and then updated at hourly intervals during a
234 5-day period ending at 00 UTC on 21 May 2014.

235 Atmospheric prognostic variables in the COSMO model include the horizontal and meridional
236 wind components, temperature, pressure, and the mixing ratios for water vapor, cloud water, rain-
237 water, pristine ice, snow, and graupel. Cloud microphysical processes, such as autoconversion,
238 accretion, and self-collection, are represented using a simplified version of the Seifert and Be-
239 heng (2001) double-moment microphysics scheme that was reduced to a single-moment scheme
240 for computational efficiency. Cloud formation and decay processes are parameterized based on
241 the work of Lin et al. (1983). Heating rates due to radiative effects are updated at 15-min in-
242 tervals using the δ -2-stream method developed by Ritter and Geleyn (1992). Deep convection
243 is explicitly resolved whereas shallow convection is parameterized using a simplified version of
244 the Tiedtke (1989) mass-flux scheme. A 2.5 order turbulent kinetic energy scheme developed by
245 Raschendorfer (2001) is used to predict turbulence.

246 After an initial 12-h spin-up period, simulated SEVIRI brightness temperatures were generated
247 for each ensemble member and the deterministic run at hourly intervals during a 4.5-day period
248 from 13 UTC 16 May 2014 to 00 UTC 21 May 2014 using first-guess model output from 1-h

249 COSMO-DE forecasts. The model profiles were interpolated to the thinned SEVIRI observation
250 locations, and then simulated 6.2 μm and 7.3 μm brightness temperatures were computed using
251 version 10.2 of the RTTOV radiative transfer model (Saunders et al. 1999). RTTOV includes an
252 enhanced cloud-scattering module that enables the use of cloud profiles located on the NWP model
253 vertical grid (Matricardi 2005; Hocking et al. 2011). When computing cloudy brightness temper-
254 atures, RTTOV requires vertical profiles of liquid water content, ice water content, and fractional
255 cloud cover. These quantities were computed using the COSMO model output and empirical rela-
256 tionships developed by Kostka et al. (2014). The default maximum-random cloud overlap scheme
257 in RTTOV based on Raisanen (1998) was used during this study. RTTOV also includes several
258 options to diagnose the ice particle effective diameters from the forecast ice water content based
259 on relationships developed by Wyser (1998), Ou and Liou (1995), and McFarquhar et al. (2003)
260 along with two ice crystal shape options (aggregates and randomly-oriented hexagonal crystals)
261 that together are used to compute the ice radiative properties. For this study, we assume hexagonal
262 ice crystals and compute the particle diameters using the McFarquhar et al. (2003) method. These
263 settings were chosen because they provided the smallest overall bias during the 108-h study pe-
264 riod based on six sensitivity experiments using the various ice crystal diameter and shape options.
265 The mean brightness temperature for ice clouds between the best and worst options differed by
266 approximately 1 K for the 6.2 μm band and 2.5 K for the 7.3 μm band during the entire study
267 period (not shown), which illustrates the large uncertainty associated with the ice cloud property
268 lookup tables in RTTOV.

269 **3. Nonlinear Bias Correction (NBC) Method**

270 Traditional BC methods remove biases between a given set of observed and model-equivalent
271 satellite brightness temperatures through use of a set of BC predictors that describe the atmospheric

272 state or characteristics of the satellite data. Both static and VarBC methods typically assume that
273 a linear relationship exists between the departure bias and a given set of predictors or that a global
274 constant can be added to the observations. This linear BC approach has been shown to work well
275 for clear-sky observations possessing Gaussian error characteristics for which a set of constant and
276 linear BC coefficients are sufficient to remove the bias; however, their use will be sub-optimal if
277 the observation bias varies as a nonlinear function of some predictor. For satellite observations,
278 nonlinear error dependencies are more likely to occur when cloudy observations are assimilated
279 given the prevalence of nonlinear processes in clouds that could lead to complex errors in the fore-
280 cast cloud field and the possibility that nonlinear error sources could be introduced by the forward
281 radiative transfer model used to compute the model-equivalent brightness temperatures. For exam-
282 ple, with infrared brightness temperatures, it is possible that increased uncertainty simulating ice
283 radiative properties in forward radiative transfer models could lead to biases that are a nonlinear
284 function of some cloud property, such as cloud top height. Thus, given the increased interest in
285 all-sky DA, it is desirable to develop BC methods that can remove both linear and nonlinear bias
286 components from the innovations.

287 One method that can be used to account for nonlinear error dependencies in a set of observations
288 is a Taylor series polynomial expansion that includes higher order terms that can capture nonlinear
289 features of the error distribution if they exist. For a given set of observed and model-equivalent
290 brightness temperatures corresponding to a specific satellite sensor and band, the observation de-
291 parture vector is defined as:

$$\mathbf{dy} = \mathbf{y} - H(\mathbf{x}), \quad (1)$$

292 where \mathbf{y} is the observation vector, \mathbf{x} is the NWP model state vector, and $H(\mathbf{x})$ is the observation
293 operator that is used to compute the model equivalent brightness temperatures. If we assume that
294 the bias in the observation departures can be described by a real function $f(z)$ of a single variable

295 (e.g., predictor) that is infinitely differentiable around a real number c , Eqn. 1 can be decomposed
 296 into an N order Taylor series expansion:

$$\mathbf{dy} = \left(f(c) + \frac{f'(c)(z^{(i)} - c)}{1!} + \frac{f''(c)(z^{(i)} - c)^2}{2!} + \frac{f'''(c)(z^{(i)} - c)^3}{3!} + \dots + \frac{f^{(n)}(c)(z^{(i)} - c)^n}{n!} \right)_{i=1, \dots, m} \quad (2)$$

297 where \mathbf{dy} is the $m \times 1$ observation departure vector and m is the number of observations, $f^{(n)}(c)$ is
 298 the n th derivative of f evaluated at the point c , and $z^{(i)}$ is the predictor value for the i th observation.
 299 The $i = 1, \dots, m$ notation outside the parentheses indicates that the Taylor series approximation is
 300 computed separately for each element of the \mathbf{dy} vector using the equation within the parentheses.
 301 The variable used as the predictor is chosen based on its ability to capture some aspect of the
 302 observation departure bias, whereas the value $z^{(i)}$ of that variable for a given observation can be
 303 obtained from a variety of sources, such as the model background or a satellite retrieval. The
 304 constant c can be set to any value because $c + \delta c$ simply moves c to another constant value;
 305 therefore, for convenience, we define c to be the mean of the predictor values:

$$c = \frac{\sum_{i=1}^m z^{(i)}}{m} \quad (3)$$

306 It is readily apparent from Eqn. 2 that the higher order terms represent nonlinear components be-
 307 cause the exponents are ≥ 2 , with the $(z - c)^2$ and $(z - c)^3$ polynomials representing the quadratic
 308 and cubic terms, respectively.

309 The single variable case shown in Eqn. 2 can subsequently be generalized to be a function of
 310 more than one predictor:

$$\begin{aligned}
\mathbf{dy} = & \left(f(a_1, \dots, a_d) + \sum_{j=1}^d \frac{\partial f(a_1, \dots, a_d)}{\partial x_j} (x_j^{(i)} - a_j) \right. \\
& + \frac{1}{2!} \sum_{j=1}^d \sum_{k=1}^d \frac{\partial^2 f(a_1, \dots, a_d)}{\partial x_j \partial x_k} (x_j^{(i)} - a_j)(x_k^{(i)} - a_k) \\
& \left. + \frac{1}{3!} \sum_{j=1}^d \sum_{k=1}^d \sum_{l=1}^d \frac{\partial^3 f(a_1, \dots, a_d)}{\partial x_j \partial x_k \partial x_l} (x_j^{(i)} - a_j)(x_k^{(i)} - a_k)(x_l^{(i)} - a_l) + \dots \right)_{i=1, \dots, m}
\end{aligned} \quad (4)$$

311 which can be written more compactly as:

$$\mathbf{dy} = \left(\sum_{n_1=0}^d \dots \sum_{n_d=0}^d \left(\frac{\partial^{(n_1+\dots+n_d)} f}{\partial x_1^{n_1} \dots \partial x_d^{n_d}} \right) (a_1, \dots, a_d) \frac{(x_1^{(i)} - a_1)^{n_1} \dots (x_d^{(i)} - a_d)^{n_d}}{n_1! \dots n_d!} \right)_{i=1, \dots, m}, \quad (5)$$

312 where d is the number of predictors, $f^{(n_d)}(a_d)$ denotes the n th partial derivative of f evaluated at
313 the point a_d , and $x_d^{(i)}$ is the i th value for a given predictor x_d .

314 For illustrative purposes, if we assume a single variable, third order Taylor series expansion for
315 a single satellite sensor and band, and define the BC coefficients such that $b_n = \frac{f^{(n)}(a)}{n!}$, Eqn. 2 can
316 be written as:

$$\mathbf{dy} = \left(b_0 + b_1(z^{(i)} - c) + b_2(z^{(i)} - c)^2 + b_3(z^{(i)} - c)^3 \right)_{i=1, \dots, m} \quad (6)$$

317 or alternatively in matrix notation as:

$$\mathbf{dy} = \mathbf{A}\mathbf{b} \quad (7)$$

318 where \mathbf{dy} is the $m \times 1$ observation departure vector, \mathbf{A} is an $m \times n$ matrix containing the n Taylor
319 series terms $(z^{(i)} - c)^l$ for each i th observation, where $l = 0, \dots, n-1$, and \mathbf{b} is an $n \times 1$ vector con-
320 taining the BC coefficients. This is an overdetermined system of m linear equations in n unknown
321 coefficients because $m > n$. The first column of \mathbf{A} contains ones, with the remaining columns con-
322 taining the linear and higher order Taylor series terms. Because this kind of system typically does
323 not have an analytic solution, we instead want to find the coefficients \mathbf{b} that best fit the equations
324 by solving the quadratic minimization problem $\hat{\mathbf{b}} = \min_b S(\mathbf{b})$, where the objective function S is

325 given by:

$$S(b) = \sum_{i=1}^m |dy_i - \sum_{j=1}^n A_{ij}b_j|^2 = \|\mathbf{dy} - \mathbf{Ab}\|^2 \quad (8)$$

326 and $\|\cdot\|$ is the Euclidean norm. Because most real-world phenomena act as a low pass filter in the
 327 forward direction where \mathbf{A} maps \mathbf{b} to \mathbf{dy} , the inverse mapping will operate as a high-pass filter that
 328 amplifies noise and can therefore lead to a poorly conditioned problem. Preference, however, can
 329 be given to smaller norms by adding a Tikhonov regularization term, $\|\Gamma\mathbf{b}\|^2$, to Eqn. 8, which is a
 330 standard approach when solving inverse problems (Nakamura and Potthast, 2015). For simplicity,
 331 we choose a matrix that is a multiple of the identity matrix ($\Gamma = \alpha I$), such that:

$$\hat{S}(b) = \|\mathbf{dy} - \mathbf{Ab}\|^2 + \alpha \|\mathbf{Ib}\|^2 \quad (9)$$

332 Sensitivity tests showed that α could be set to a very small value (10^{-9}) when one variable was
 333 used in the regression; however, a slightly larger value (10^{-6}) was found to work better for the
 334 multivariate regressions. These values were used for the univariate and multivariate experiments
 335 presented in Section 4. The least squares solution can then be found by differentiating \hat{S} with
 336 respect to b , and equating to 0, such that:

$$\frac{\partial \hat{S}}{\partial b} = \mathbf{A}^T \mathbf{dy} - (\alpha I + \mathbf{A}^T \mathbf{A}) \mathbf{b} = 0, \quad (10)$$

337 or alternatively, after rearranging and multiplying both sides of Eqn. 10 by $(\alpha I + \mathbf{A}^T \mathbf{A})^{-1}$, we can
 338 solve for the b vector containing the BC coefficients using:

$$\mathbf{b} = (\alpha I + \mathbf{A}^T \mathbf{A})^{-1} \mathbf{A}^T \mathbf{dy} \quad (11)$$

339 where $(\alpha I + \mathbf{A}^T \mathbf{A})$ is a symmetric, square matrix with dimensions $n \times n$. The small dimensions of
 340 this matrix make it easy to compute its inverse, thereby making it feasible to include higher order
 341 Taylor series terms, additional predictors, and a large OMB departure dataset when computing the
 342 BC coefficients. After solving for \mathbf{b} , which is done separately for each satellite band and sensor,

343 the BC coefficients can then be applied to \mathbf{dy} to remove the linear and nonlinear conditional bias
344 components from the observations.

345 **4. Results**

346 In this section, the ability of the NBC method to remove biases from all-sky satellite infrared
347 brightness temperatures is assessed using OMB departure statistics accumulated at hourly intervals
348 during a 4.5 day period in which conventional observations were actively assimilated and SEVIRI
349 observations were passively monitored. Figure 1 shows the evolution of the observed SEVIRI 6.2
350 μm brightness temperatures during this time period. At the start of the period on 16 May (Fig.
351 1a), an area of cold upper level clouds associated with a band of precipitation was located across
352 the eastern half of the domain. This weather feature slowly weakened over Germany during the
353 next two days (Fig. 1b, c), with the brightness temperatures becoming warmer as the convective
354 clouds were replaced by cirrus and mid-level clouds. Generally clear skies characterized by warm
355 brightness temperatures were also present across parts of the domain during this time period, with
356 clear skies prevailing across most of the region on 19 May (Fig. 1d). A large area of convection
357 with very cold upper-level clouds then moved into the western half of the domain on 20 May (Fig.
358 1e). Overall, it is evident that the study period contains a wide range of atmospheric conditions
359 and cloud types that supports a realistic assessment of the NBC method during the warm season.

360 *a. Univariate Bias Correction Results*

361 To explore the ability of individual predictors to remove the bias from all-sky infrared obser-
362 vations, univariate NBC experiments were performed using the satellite zenith angle and various
363 predictors sensitive to clouds and WV, such as the brightness temperature, cloud top height, and
364 integrated water content over some vertical layer. This section presents results from a subset of

365 these experiments that remove the bias from all-sky SEVIRI 6.2 μm observations. The impact of
366 each predictor is assessed using OMB departure distributions normalized by the standard deviation
367 in a given sample and with 2-D probability distributions of the departures plotted as a function of
368 a given predictor. The results are evaluated separately for the original departure distribution and
369 for distributions for which the bias has been removed using either a 0th (constant), 1st (linear),
370 2nd (quadratic), or 3rd (cubic) order Taylor series polynomial expansion.

371 1) OBSERVED BRIGHTNESS TEMPERATURE PREDICTOR

372 As shown by the probability distributions in Fig. 2, the observed 6.2 μm brightness temperatures
373 are an excellent predictor of their own bias, especially when higher order Taylor series terms are
374 used. The horizontal magenta line in each panel depicts the mean bias of the entire distribution,
375 whereas the shorter horizontal black lines depict the conditional bias in each column and will
376 be used to assess how the bias varies as a function of the predictor value. This terminology is
377 being used to differentiate biases conditioned on the predictor value from the bias of the overall
378 distribution. For example, though each distribution except for the original distribution will have
379 zero overall bias, this obscures the fact that the conditional bias could potentially vary as a function
380 of the predictor value. Inspection of Fig. 2a reveals a nonlinear pattern in the conditional biases,
381 with a tendency for the simulated brightness temperatures to be too warm (cold) when the observed
382 brightness temperatures are colder (warmer) than 235 K. Though the mean bias of the distribution
383 is relatively small (-0.83 K), the nonlinear pattern in the conditional biases means that constant
384 and linear BC terms alone will be unable to remove all of the bias. For example, even though the
385 constant BC term removes the mean bias from the distribution (Fig. 2b), its shape remains the
386 same and therefore large conditional biases remain throughout the distribution. Likewise, the 1st
387 order BC term removes the linear departure component by raising (lowering) the cold (warm) end

388 of the distribution, which reduces the conditional biases for the coldest brightness temperatures,
389 but turns a positive bias into a negative bias for the warmest brightness temperatures (Fig. 2c).
390 Removal of the constant and linear bias components exposes an asymmetric arch shape in the
391 conditional biases that is largely removed when the 2nd order quadratic term is used (Fig. 2d),
392 except for nonzero biases that remain at the cold and warm ends of the distribution. Finally, when
393 the 3rd order cubic term is used, the general shape of the distribution is unchanged; however, it
394 is evident that subtle improvements were made to it given that most of the conditional biases are
395 now close to zero. Together, these results show that even though each BC distribution has zero
396 mean bias, that the conditional biases in the distribution are much smaller when the higher order,
397 nonlinear BC terms are applied to the observations.

398 Normalized OMB departure histograms computed using the original observations and the con-
399 stant, 1st, 2nd, and 3rd order BC observations are shown in Fig. 3a-e. Each histogram is nor-
400 malized based on its variance, with the curved red line on each panel representing a Gaussian
401 distribution with zero mean and a variance equal to that of the sample. Overall, the variance and
402 root mean square error (RMSE) are greatly reduced when the 1st order BC coefficients are ap-
403 plied to the observations (Fig. 3c), which is primarily due to the smaller departures for the colder
404 brightness temperatures (e.g. Fig. 2c). The variance was further reduced when the 2nd order BC
405 was used, with only minimal changes occurring when this was expanded to a 3rd order BC (Figs.
406 3d, e). The fact that the higher order terms only had a small impact on these statistics while simul-
407 taneously having a large positive impact on the conditional biases in Fig. 2 illustrates that more
408 detailed analysis methods such as 2-D probability distributions can provide additional insight into
409 the characteristics of the OMB departure distributions. Comparison of the histograms also shows
410 that the negative skewness in the original distribution (Fig. 3a) changes to positive skewness after
411 the BC terms are applied. This behavior primarily results from a conditional positive skewness for

412 brightness temperatures < 230 K that is evident in Fig. 2a by the tendency for the conditional bias
413 in each column to be located above the bin with the maximum probability. Because the same BC
414 is applied to a given brightness temperature regardless of its OMB departure, the positive skew-
415 ness in the conditional distributions is preserved as they are shifted upward, thereby leading to a
416 positive skewness in the full BC distributions.

417 2) CLOUD TOP HEIGHT PREDICTOR

418 Because infrared observations are very sensitive to the vertical distribution of clouds, an experi-
419 ment was performed using the NWC SAF cloud top height retrievals as the BC predictor to better
420 isolate the impact of clouds. To provide complete domain coverage, the clear-sky observations
421 were assigned a height equal to the model terrain elevation. Overall, the conditional biases in the
422 original distribution (Fig. 4a) are close to zero for cloud top heights < 7 km; however, the biases
423 increase for clouds above this level and peak near -6 K for cloud top heights > 10 km. This is a
424 complex error pattern that a constant BC scheme is unable to fix (Fig. 4b). Indeed, the upward shift
425 of the distribution to remove the mean bias actually worsens the conditional biases for cloud top
426 heights < 7 km, while leading to only minor improvements for the upper-level clouds. The linear
427 correction (Fig. 4c) slightly improves the conditional biases for lower and upper-level clouds, but
428 worsens the bias for mid-level clouds, which together slightly reduces the variance in the overall
429 distribution (Fig. 3f). Use of the 2nd order quadratic term substantially improves the distribution
430 by removing the arch in the conditional bias pattern by decreasing the magnitude of the positive
431 (negative) OMB departures for cloud tops located in the middle (upper) troposphere (Fig. 4d).
432 These changes resulted in a much smaller variance in the histogram (Fig. 3g). As was the case in
433 the previous section, the 3rd order BC led to slightly smaller conditional biases across most of the
434 distribution (Fig. 4e), but had minimal impact on the statistics of the overall distribution (Fig. 3h).

435 Though the cloud top height predictor was unable to reduce the variance of the full distribution
436 as much as the brightness temperature predictor did, the NBC method was still able to greatly
437 improve the distribution by decreasing the conditional biases. Its use also led to a more symmetric
438 OMB departure distribution (Fig. 3h). These results show that cloud top height information can
439 be used to remove the bias from all-sky infrared observations if higher order Taylor series terms
440 are used.

441 3) VERTICALLY-INTEGRATED WATER CONTENT PREDICTOR

442 In this section, the impact of using a BC predictor that depicts the total water content over a
443 vertical layer is assessed. Numerous experiments were performed using different vertical layers;
444 however, for brevity, results are only shown for the predictor that encapsulates the total water
445 content between 100 and 700 hPa because that is the portion of the atmosphere where $6.2 \mu\text{m}$
446 brightness temperatures are most sensitive. Unlike the previous predictors, this predictor is com-
447 puted using model output. The total water content is calculated for each ensemble member by
448 converting the WV and all cloud hydrometeor mixing ratios in each model layer into mm and
449 then integrating over the 100-700 hPa layer. Inspection of Fig. 5a shows that this predictor has
450 a less complex OMB departure pattern than occurred when the cloud top height and brightness
451 temperatures were used as the predictors. There are however slightly larger biases on both ends of
452 the distribution, with a small upward slope in the maximum probabilities as the total water content
453 increases. This linear error trend is removed by the linear bias correction term (Fig. 5c), which
454 reduces the conditional biases when the total water content is < 7 mm, but increases it elsewhere.
455 The subtle arch in the conditional biases is subsequently removed after applying the 2nd order
456 quadratic term (Fig. 5d), with only minor changes occurring after the 3rd order term is used (Fig.
457 5e). Comparison of the histograms (Figs. 3i-k) shows that the total water predictor had only a

458 small impact on the variance of the full distribution; however, the scatterplots showed that it still
459 improved the conditional bias across most of the distribution. Even so, this predictor still had
460 a much smaller impact than the previous predictors that were directly sensitive to the cloud top
461 height, which indicates that the location of the cloud top rather than the vertically integrated cloud
462 and WV content is a more effective BC predictor for all-sky infrared brightness temperatures.

463 4) SATELLITE ZENITH ANGLE PREDICTOR

464 Given that the satellite zenith angle is widely used in operational BC methods, an additional
465 experiment was performed using it as the BC predictor. After adjusting for the mean bias in the
466 original distribution, the conditional biases are close to zero across the entire distribution, with
467 only a slight downward trend in the bias for zenith angles $> 48^\circ$ (Fig. 6b). Application of the
468 1st to 3rd order BC terms (Figs. 6c-e) eliminated most of these conditional biases; however, the
469 impact of this predictor on the statistics of the entire distribution was negligible according to the
470 histograms (Figs. 3l-n). These results indicate that the bias in the observations is only very weakly
471 related to the satellite zenith angle; however, the small improvements made to the conditional
472 biases by the 2nd to 3rd order terms also show that there is a small nonlinear bias component that
473 can be removed when using this predictor.

474 *b. Clear and Cloudy Sky Error Evaluation*

475 Next, the relative impact of the linear and nonlinear BC terms on the clear and cloudy-sky obser-
476 vations is examined more closely using a subset of the $6.2 \mu\text{m}$ brightness temperatures for which
477 both the model background and a given observation were identified as being clear or cloudy. Each
478 observation was classified as clear or cloudy based on the NWC SAF cloud mask dataset whereas
479 each model grid point was deemed to be clear (cloudy) if the sum of all cloud hydrometeor mixing

480 ratios over the entire vertical profile was less (greater) than 10^{-6} kg kg⁻¹. The 2-D probability
481 distributions for the clear-sky matched observations are shown in Fig. 7, with the corresponding
482 histograms shown in Fig. 8. The observed 6.2 μ m brightness temperatures were used as the BC
483 predictor. Inspection of Fig. 7a reveals that the original distribution contains both a systematic
484 bias and a large linear trend where mostly negative OMB departures for the colder brightness tem-
485 peratures transition into mostly positive departures for the warmer brightness temperatures. The
486 linear trend indicates that the WV field in the model background is more uniform than observed
487 such that the model tends to be too wet (dry) in regions where the observations indicate less (more)
488 WV. Overall, most of the bias is removed from the clear-sky observation departures using only the
489 constant and 1st order terms, with little or no impact due to the higher order terms (Figs. 7b-e).
490 This behavior is consistent with existing BC schemes that use constant and linear corrections to
491 remove the bias from clear-sky observation departures.

492 For the cloud-matched observations shown in Figs. 9 and 10, the NWC SAF cloud top height
493 retrievals were used as the predictor. The OMB departure pattern and conditional biases for these
494 observations are very similar to that shown in Fig. 4 when both clear and cloudy-sky observations
495 were included in the regression. This includes the generally positive departures for mid-level
496 clouds and the transition to large negative departures for the upper-level clouds (Fig. 9a). Large
497 departures remained in the distribution for all cloud top heights after the constant and linear BC
498 terms were applied to the observations (Fig. 9c). It is only when the 2nd and 3rd order terms are
499 used that the conditional biases become close to zero throughout the entire distribution (Figs. 9d,
500 e). The histograms in Fig. 10 also reveal that the quadratic and cubic terms had a much larger
501 impact on the overall statistics than occurred for the clear-sky matched observations. These results
502 provide further evidence that the nonlinear conditional biases evident in the all-sky scatterplots in
503 Section 4.1 primarily result from biases associated with the cloudy observations. It also shows

504 that the NBC method is an effective method to remove both linear and nonlinear biases from all-
505 sky infrared brightness temperature departures if a suitable cloud-sensitive variable is used as the
506 predictor.

507 *c. Multivariate Bias Correction Results*

508 In addition to the univariate NBC experiments discussed in previous sections, multivariate ex-
509 periments were performed to assess the impact of using more than one predictor to remove the ob-
510 servation bias. For a 3rd order polynomial expansion using two variables, it is necessary to solve
511 for seven coefficients in Eqn. 11, whereas 22 coefficients are computed when three predictors are
512 used. Because a direct approach is used to simultaneously estimate all of the BC coefficients, it
513 is not possible to determine the individual contribution of each predictor on the OMB departures;
514 however, the total contribution of all of the predictors within a given Taylor series order (e.g., 1st,
515 2nd, and 3rd) can still be inferred through comparison of the results obtained using different order
516 expansions. Though using more than one variable greatly increases the size of the A matrix, it is
517 still computationally efficient to solve for the inverse of $A^T A$ given its small dimensions.

518 Numerous experiments using different predictor combinations and a 2nd or 3rd order poly-
519 nomial expansion were performed; however, for brevity, this section only includes results from the
520 combination that had the largest impact on the OMB departure distributions. This particular con-
521 figuration employed a 3rd order expansion with the satellite zenith angle, 100-700 hPa total water
522 content, and observed brightness temperatures for a given satellite band used as the BC predic-
523 tors for that band. A separate multi-variate experiment (not shown) that employed the cloud top
524 height rather than the brightness temperature as the third predictor revealed that it had a smaller
525 impact, similar to what occurred with the univariate experiments shown earlier. There may be
526 some overlap between the brightness temperature and satellite zenith angle predictors; however,

527 this should be minimal because the zenith angle predictor primarily accounts for potential biases
528 in the radiative transfer model associated with the path length through the atmosphere, whereas the
529 brightness temperature predictor is being used as a proxy for the cloud top height given its strong
530 sensitivity to the cloud top. Unlike the previous sections that focused exclusively on the 6.2 μm
531 band, this section presents results from experiments that removed the bias from both of the SE-
532 VIRI WV-sensitive bands (e.g., 6.2 μm and 7.3 μm). All observations, both clear and cloudy-sky,
533 were used during these experiments.

534 1) SEVIRI 6.2 μm EXAMPLE

535 Figure 11 shows the OMB departure distributions for the 6.2 μm multivariate NBC experiment,
536 with the corresponding normalized histograms shown in Figs. 3o-q. Comparison to Fig. 2 shows
537 that the departure distributions for the multivariate case are similar to those from the univariate
538 case employing only the observed brightness temperature as the BC predictor. This is not sur-
539 prising given that the experiments employing the satellite zenith angle and total water content
540 predictors both had a much smaller impact on the distributions (Figs. 5, 6). Overall, the shape
541 of the distribution is improved after the linear term is used; however, there are still large condi-
542 tional biases at both ends of the distribution (Fig. 11c). The arch pattern in the conditional bias
543 was subsequently removed after the quadratic term was applied (Fig. 11d), with slightly smaller
544 (larger) biases occurring at the warm (cold) end of the distribution after using the 3rd order cubic
545 term (Fig. 11e). Though the distributions are similar to those shown in Fig. 2, it is evident that the
546 width of the conditional distribution is less for all predictor values. This is encouraging because
547 it shows that even though the impact of the satellite zenith angle and total water content predic-
548 tors was relatively small when used individually, they still provided new information that further
549 reduced the OMB departures when used in combination with the observed brightness temperature

550 predictor. Inspection of the histograms (Figs. 3o-q) shows that the variance was greatly reduced
551 compared to the univariate experiments; however, each of the distributions had a large positive
552 skewness similar to that seen in Figs. 3c-e when the brightness temperature was used as the BC
553 predictor. It is important to note however that quality control measures could potentially be used to
554 reduce the skewness in the distribution after the BC terms are applied. This topic will be explored
555 in a future study.

556 2) SEVIRI 7.3 μM EXAMPLE

557 In this section, we assess the ability of the multivariate NBC method to improve the observation
558 error characteristics of the 7.3 μm band. As discussed in Section 2.1, observations from this band
559 are sensitive to WV and clouds in the middle and upper troposphere, with a weighting function that
560 peaks near 500 hPa in clear sky scenes. Overall, each of the OMB departure distributions (Fig.
561 12) have shapes that are similar to the corresponding 6.2 μm distributions (Fig. 11); however,
562 their error range is larger because the weighting function for this band peaks at a lower level
563 in the troposphere, thereby leading to potentially larger departures due to mismatched clouds in
564 the observations and model background. Though the linear BC term substantially improves the
565 distribution by making the departures less negative for colder brightness temperatures, non-zero
566 conditional biases remain across most of the distribution, with negative (positive) biases occurring
567 for brightness temperatures colder (warmer) than 230 K (Fig. 12c). As occurred in the previous
568 experiments, the conditional biases are almost eliminated after the 2nd order BC term is used,
569 with minimal changes occurring due to the 3rd order term (Figs. 12d, e). The negative skewness
570 present in the original histogram (Fig. 13a) switches to a large positive skewness after the linear
571 BC term is used (Fig. 13c). Inspection of the OMB departure distributions shows that the positive
572 skewness developed in response to the large upward shift in the conditional distributions for the

573 colder brightness temperatures (Fig. 12a) that exposed the conditional positive skewness in the
574 original distribution for warmer brightness temperatures that was being masked in the overall
575 histogram by the large negative OMB departures. Another notable feature of the histograms is
576 that their peaks are higher and narrower than the 6.2 μm histograms (Figs. 3o-q). This strongly
577 non-Gaussian behavior was already present in the original histogram and is likely due to the large
578 percentage of clear-sky observations containing small departures combined with fatter tails due
579 to cloud displacement errors. Even so, these results show that the NBC method improved the
580 distribution such that the variance was much lower and the conditional biases were reduced to
581 near zero across most of the distribution. Also, as was the case with the 6.2 μm band, the linear
582 BC term had the largest impact on the overall statistics; however, the variance was also reduced
583 when using the higher order nonlinear BC terms.

584 **5. Discussion and Conclusions**

585 In this study, output from a high-resolution, regional-scale ensemble DA system was used to
586 explore the ability of an innovative method to remove the bias associated with all-sky satellite
587 infrared brightness temperatures using a Taylor series polynomial expansion of the OMB departures.
588 This so-called NBC method uses OMB statistics accumulated over some period of time to
589 remove linear and nonlinear conditional biases in a distribution through use of higher order Taylor
590 series terms and a set of BC predictors. Nonlinear conditional biases can be identified using 2nd
591 (quadratic) and 3rd (cubic) order terms (and even higher order terms if desired), whereas the constant
592 and linear bias components can be diagnosed using the 0th and 1st order terms, respectively.

593 The ability of the NBC method to effectively remove the bias associated with all-sky SEVIRI
594 infrared brightness temperatures was assessed using output from high-resolution ensemble DA
595 experiments performed using the KENDA system. OMB departure statistics for the 6.2 and 7.3

596 μm bands sensitive to clouds and WV in the upper and middle troposphere, respectively, were
597 accumulated at hourly intervals during a 108-h period from 16-21 May 2014 using output from
598 the COSMO-DE domain that covers Germany and surrounding areas with 2.8-km horizontal grid
599 spacing. Conventional observations were actively assimilated, whereas the SEVIRI observations
600 were passively monitored and therefore did not affect the analyses during the hourly assimila-
601 tion cycles. Model-equivalent brightness temperatures were computed for each observation and
602 ensemble member using the RTTOV radiative transfer model. The study period contained both
603 clear-sky areas and a wide range of cloud types that together promoted a realistic assessment of
604 the NBC method during the warm season.

605 Univariate and multi-variate NBC experiments were performed using the satellite zenith angle
606 and other predictors sensitive to clouds and WV, with their impact on the conditional bias and other
607 aspects of the OMB departure distributions assessed using normalized histograms and probability
608 distributions plotted as a function of the predictor. Overall, the results revealed that there are often
609 strongly nonlinear conditional bias patterns in the OMB probability distributions that cannot be
610 removed using only constant and linear BC terms. Though the overall bias of each distribution is
611 equal to zero regardless of the order of the Taylor series expansion, there are often large conditional
612 biases that vary as a function of the BC predictor. Because each SEVIRI band had a relatively
613 small systematic bias, the constant BC term only had a small impact on the distributions. The
614 linear 1st order term generally had the largest impact on the statistics of the entire distribution
615 as measured by reductions in the variance; however, conditional biases often remained across
616 much of the distribution. These conditional biases were typically reduced to near zero across
617 the entire distribution only after the nonlinear 2nd and 3rd order terms were applied to the OMB
618 departures. Indeed, the conditional bias patterns often exhibited an arch shape for which the
619 2nd order quadratic term is ideally suited to remove. The tendency for the nonlinear terms to

620 have a small impact on the variance of the entire distribution while simultaneously having a large
621 positive impact on the conditional biases also illustrates that detailed analysis methods such as 2-D
622 probability distributions provide valuable insight into the behavior of the BC method that is not
623 possible using traditional 1-D error histograms.

624 Inspection of the univariate NBC results showed that the variance of the BC distributions was
625 smallest when the brightness temperature observations were used as the BC predictor. The vari-
626 ance was also substantially reduced when the NWC SAF cloud top height retrievals were used as
627 the predictor. Both of these predictors were able to diagnose and remove nonlinear biases asso-
628 ciated with the cloudy observations. For example, large positive conditional biases for mid-level
629 clouds transitioned into large negative conditional biases for upper-level clouds. Though not ex-
630 amined during this study, the different signs of the conditional biases for these clouds could be
631 related to the ability of the COSMO model and RTTOV to properly simulate ice and mixed-phase
632 cloud properties. The experiments using the satellite zenith angle or vertically-integrated water
633 content showed that these BC predictors had a much smaller impact on the variance of the over-
634 all distribution. This behavior indicates that variables sensitive to the cloud top height are more
635 effective BC predictors for all-sky infrared brightness temperatures, especially when higher order
636 Taylor series terms are included. Even so, the multivariate experiments showed that though the
637 zenith angle and total water content predictors only had a relatively small impact on the departure
638 histograms when used individually, they still provided new information that greatly reduced the
639 variance of the distribution when used in combination with the observed brightness temperature
640 predictor.

641 Additional univariate NBC experiments were performed to examine the influence of linear and
642 nonlinear components on the OMB departure distributions for clear- and cloudy-sky observations
643 using a subset of the $6.2 \mu\text{m}$ brightness temperatures for which both a given observation and the

644 corresponding model grid point were identified as being clear or cloudy. Overall, comparisons of
645 the statistics for the clear-sky and cloudy-sky matched observations revealed that nonlinear error
646 sources are much more important for cloudy sky observations as signified by the much larger
647 impact of the 2nd and 3rd order Taylor series terms on the variance and the conditional biases
648 in the distributions. For the clear-sky observations, the conditional biases could be effectively
649 removed using only the 0th and 1st order terms, which is consistent with existing operational BC
650 methods that typically remove the bias from clear-sky satellite observations using a set of constant
651 and linear BC coefficients. These results show that the nonlinear conditional bias patterns evident
652 in the all-sky OMB departure distributions primarily resulted from nonlinear biases in the cloudy-
653 sky infrared brightness temperatures. They also show that the NBC method can effectively remove
654 both linear and nonlinear conditional biases from all-sky infrared brightness temperatures provided
655 that a suitable cloud-sensitive variable is used as one of the predictors.

656 Future work includes running cycled DA experiments using the KENDA system to assess the
657 impact of the NBC method on the forecast accuracy when assimilating clear- and cloudy-sky in-
658 frared brightness temperatures. Additional experiments will be necessary to explore the ability of
659 the method to remove biases from the OMB departures when the simulated brightness tempera-
660 tures and cloud top heights are used as the BC predictors rather than their observed counterparts.
661 Preliminary results indicate that predictors derived from the NWP model cloud field rather than the
662 observations have a smaller impact on the overall statistics as measured by reductions in variance;
663 however, they were still able to effectively remove the conditional biases across most of the dis-
664 tribution when higher order Taylor series terms were used. These results also indicate that it may
665 be necessary to use up to a 4th order polynomial to remove the bias if the NWP-derived quantities
666 are used rather than their observed counterparts. A more detailed assessment of this sensitivity
667 is currently underway. Additional experiments will also be necessary to explore the ability of the

668 NBC method to remove biases from infrared bands that are sensitive to the land surface or other
669 atmospheric constituents such as ozone, as well as for all-sky microwave and visible radiances.

670 Though the NBC method used in this paper was implemented as a static, off-line method, it
671 could also be incorporated into online methods such as VarBC through inclusion of additional
672 nonlinear predictors. For example, the VarBC system at the Met Office uses Legendre polynomial
673 predictors to remove residual scan biases and Fourier predictors to correct complex orbital biases
674 in some satellite sensors (Cameron and Bell, 2016). Higher order predictors, such as the quadratic
675 form of the temperature lapse rate and 4th order polynomial of the satellite angle bias, are also
676 widely used in operational VarBC systems. Zhu et al. (2015) recently showed that inclusion of
677 a quadratic aircraft ascent/descent term reduced the bias when assimilating aircraft temperature
678 observations. Results from the current study could be used to help inform the development of
679 operational DA systems as they continue to expand into all-sky satellite DA. Finally, many of the
680 all-sky OMB departure distributions exhibited narrow peaks and fat tails that could potentially be
681 better represented using a Huber norm (Huber 1972) representation, which has been shown to lead
682 to improved quality control and more observations being assimilated (Tavolato and Isaken 2015).
683 Further research is necessary to determine if using a Huber norm in combination with the NBC
684 method can improve existing quality control methods by identifying erroneous observations after
685 the nonlinear conditional biases have been removed from the distribution. This approach could
686 potentially preserve more cloud-affected observations where nonlinear biases are more prevalent,
687 thereby leading to additional observations being assimilated in sensitive areas of the domain.

688 *Acknowledgments.* We thank each reviewer for their prompt reviews and detailed feedback
689 that improved the manuscript. We gratefully acknowledge Jesse Stroik from the University of
690 Wisconsin-Madison and Hendrik Reich, Andreas Rhodin, Robin Faulwetter, and Axel Hutt from

691 the German DWD for their assistance porting and installing the KENDA system and basic cycling
692 (BACY) scripts to the NOAA/NESDIS/STAR "S4" supercomputer located at the University of
693 Wisconsin-Madison. The S4 supercomputer was used to perform all of the cycled DA experi-
694 ments. The lead author was partially supported by the NOAA Joint Polar Satellite System (JPSS)
695 program via CIMSS Cooperative Agreement NA15NES4320001 and by a University of Reading
696 International Research Studentship.

697 **6. References**

698 Anderson J., and S. Anderson, 1999: A Monte Carlo implementation of the nonlinear filtering
699 problem to produce ensemble assimilations and forecasts. *Mon. Wea. Rev.*, 127, 2741-2758.

700 Aravequia J.A., I. Szunyogh, E. J. Fertig, E. Kalnay, D. Kuhl, and E. J. Kostelich, 2011: Eval-
701 uation of a strategy for the assimilation of satellite radiance observations with the local ensemble
702 transform Kalman filter. *Mon. Weather Rev.*, 139, 1932-1951, doi: 10.1175/2010MWR3515.1.

703 Auligne T., A. P. McNally, and D. P. Dee, 2007: Adaptive bias correction for satellite data in a
704 numerical weather prediction system. *Q. J. R. Meteorol. Soc.*, 133, 631-642.

705 Baldauf M., A. Seifert, J. Forstner, D. Majewski, M. Raschendorfer, and T. Reinhardt, 2011:
706 Operational convective-scale numerical weather prediction with the COSMO Model: Description
707 and sensitivities. *Mon. Weather Rev.*, 139, 3887-3905.

708 Baum, B. A., P. Yang, A. J. Heymsfield, A. Bansemer, A. Merrelli, C. Schmitt, and C.
709 Wang, 2014: Ice cloud bulk single-scattering property models with the full phase matrix at
710 wavelengths from 0.2 to 100 μm . *J. Quant. Spectrosc. Radiat. Transfer*, 146, 123-139,
711 doi:10.1016/j.jqsrt.2014.02.029.

712 Cameron, J., and W. Bell, 2016: The testing and planned implementation of variational bias
713 correction (VarBC) at the Met Office. 20th International TOVS study conference, Madison,

714 WI. [https://cimss.ssec.wisc.edu/itwg/itsc/itsc20/papers/11_01_cameron_paper.](https://cimss.ssec.wisc.edu/itwg/itsc/itsc20/papers/11_01_cameron_paper.pdf)
715 pdf. Accessed 05 June 2017.

716 Cintineo, R., Otkin, J.A., Xue, M., Kong, F., 2014. Evaluating the performance of planetary
717 boundary layer and cloud microphysical parameterization schemes in convection permitting en-
718 semble forecasts using synthetic GOES-13 satellite observations. *Mon. Wea. Rev.* 142, 163-182.

719 Cintineo, R., J. A. Otkin, T. Jones, S. Koch, and D. J. Stensrud, 2016: Assimilation of syn-
720 thetic GOES-R ABI infrared brightness temperatures and WSR-88D radar observations in a high-
721 resolution OSSE. *Mon. Wea. Rev.*, 144, 3159-3180.

722 Dee, D. P., 2005: Bias and data assimilation. *Q. J. R. Meteorol. Soc.*, 131, 3323-3343, doi:
723 10.1256/qj.05.137.

724 Dee D. P., and S. Uppala, 2009: Variational bias correction of satellite radiance data in the
725 ERA-Interim reanalysis. *Q. J. R. Meteorol. Soc.* 135: 1830-1841.

726 Derber J. C., D. F. Parrish, and S. J. Lord, 1991: The new global operational analysis system at
727 the National Meteorological Center. *Weather and Forecasting*, 6, 538-547.

728 Derber, J. C., and W.-S. Wu, 1998: The use of TOVS cloud-cleared radiances in the NCEP SSI
729 analysis system, *Mon. Weather Rev.*, 126, 2287-2299.

730 Derrien M., and H. Le Gleau, 2005: MSG/SEVIRI cloud mask and type from SAF NWC. *Int.*
731 *J. Remote Sens.*, 26, 4707-4732.

732 Eikenberg, S., C. Kohler, A. Siefert, and S. Crewell, 2015: How microphysical choices affect
733 simulated infrared brightness temperatures. *Atmos. Research*, 156, 67-79.

734 Errico, R., P. Bauer, and J.-F. Mahfouf, 2007: Issues regarding the assimilation of cloud and
735 precipitation data. *J. Atmos. Sci.*, 64, 3685-3798.

736 Eyre J. R., 1992: A bias correction scheme for simulated TOVS brightness temperatures. *Techni-*
737 *cal Memorandum 176*, Reading, UK:,ECMWF.

738 Eyre, J. R., 2016: Observation bias correction schemes in data assimilation systems: a theoretic-
739 cal study of some of their properties. *J. Q. R. Meteorol. Soc.*, 142, 2284-2291.

740 Fertig E.J., S.-J. Baek, B. R. Hunt, E. Ott, I. Szunyogh, J. A. Aravequia, E. Kalnay, H. Li, and
741 J. Liu, 2009: Observation bias correction with an ensemble Kalman filter. *Tellus*, 61A, 210-226,
742 doi: 10.1111/j.1600-0870.2008.00378.x.

743 Le Gleau H., 2016: Algorithm theoretical basis document for the cloud products processors of
744 the NWC/GEO. <http://www.nwcsaf.org> (accessed 29 March 2017).

745 Harris, B. A, and G. Kelly, 2001: A satellite radiance-bias correction scheme for data assimila-
746 tion. *Q. J. R. Meteorol. Soc.*, 127, 1453-1468.

747 Hilton F., N. C. Atkinson, S. J. English, and J. R. Eyre, 2009: Assimilation of IASI at the Met
748 Office and assessment of its impact through observing system experiments. *Q. J. R. Meteorol.*
749 *Soc.*, 135, 495-505.

750 Hocking J., P. Rayer, R. Saunders, M. Matricardi, A. Geer, P. Brunet, 2011: RTTOV v10 Users
751 Guide, NWC SAF report. EUMETSAT: Darmstadt, Germany.

752 Huber P. J., 1972: Robust statistics: A review. *Ann. Math. Stat.* 43: 1041-1067.

753 Hunt B. R., E. J. Kostelich, and I. Szunyogh, 2007: Efficient data assimilation for spa-
754 tiotemporal chaos: A local ensemble transform Kalman filter. *Physica D*, 230, 112-126,
755 doi:10.1016/j.physd.2006.11.008.

756 Kostka P. M., M. Weissmann, R. Buras, B. Mayer, and O. Stiller, 2014: Observation operator
757 for visible and near-infrared satellite reflectances. *J. Atmos. Oceanic Technol.*, 31, 1216-1233.

758 Lin Y. L., R. Farley, and H. Orville, 1983: Bulk parameterization of the snow field in a cloud
759 model. *J. Climate Appl. Meteor.*, 22, 1065-1092.

760 Mahfouf, J.-F., 2010: Assimilation of satellite-derived soil moisture from ASCAT in a limited-
761 area NWP model. *Q. J. R. Meteorol. Soc.*, 136, 784-798, DOI:10.1002/qj.602.

762 Majewski, D. and coauthors, 2002: The Operational Global Icosahedral?Hexagonal Gridpoint
763 Model GME: Description and High-Resolution Tests. *Mon. Wea. Rev.*,130, 319-338.

764 Matricardi M., 2005: The inclusion of aerosols and clouds in RTIASI, the ECMWF Fast Radiative
765 Transfer Model for the Infrared Atmospheric Sounding Interferometer, Technical Memorandum
766 474, ECMWF, Reading, UK.

767 McFarquhar, G. M., S. Iacobellis, and R. C. J., Somerville, 2003: SCM simulations of tropical
768 ice clouds using observationally based parameterizations of microphysics. *J. Clim.*, 16, 1643-
769 1664.

770 Miyoshi T., Y. Sato, and T. Kadowaki, 2010: Ensemble Kalman filter and 4D-Var intercomparison
771 with the Japanese operational global analysis and prediction system. *Mon. Wea. Rev.*, 138,
772 2846-2866, doi:10.1175/2010MWR3209.1.

773 Nakamura, G., and R. Potthast, 2015: Inverse Modeling: An introduction to the theory and
774 methods of inverse problems and data assimilation. IOP Publishing, doi:10.1088/978-0-7503-
775 1218-9.

776 Okamoto, K., A. P. McNally, and W. Bell, 2014: Progress towards the assimilation of all-sky
777 infrared radiances: An evaluation of cloud effects. *Q. J. R. Meteorol. Soc.*, 140, 1603-1614,
778 doi:10.1002/qj.2242.

779 Otkin, J. A., and T. J. Greenwald, 2008: Comparison of WRF model-simulated and MODIS-
780 derived cloud data. *Mon. Wea. Rev.*, 136, 1957-1970.

781 Otkin, J. A., T. J. Greenwald, J. Sieglaff, and H.-L. Huang, 2009: Validation of a large-scale
782 simulated brightness temperature dataset using SEVIRI satellite observations, *J. Appl. Meteorol.*
783 *Climatol.*, 48, 1613-1626, doi:10.1175/2009JAMC2142.1.

784 Ou, S., and K.-N. Liou, 1995: Ice microphysics and climatic temperature feedback. *Atmos.*
785 *Res.*, 35, 127-138.

786 Parrish D. F., and J. C. Derber, 1992: The National Meteorological Center's spectral statistical
787 interpolation analysis system. *Mon. Wea. Rev.*, 120, 1747-1763.

788 Raisanen, P., 1998: Effective longwave cloud fraction and maximum-random overlap of clouds:
789 A problem and a solution. *Mon. Wea. Rev.*, 126, 3336-3340.

790 Raschendorfer M., 2001: The new turbulence parameterisation of LM. *COSMO Newsl.* 1, 89-
791 97.

792 Ritter B., and J. F. Geleyn, 1992: A comprehensive radiation scheme for numerical weather
793 prediction models with potential applications in climate simulations. *Mon. Wea. Rev.* 120, 303-
794 325

795 Saunders R., M. Matricardi, and P. Brunel, 1999: An improved fast radiative transfer model for
796 assimilation of satellite radiance observations. *Q. J. R. Meteorol. Soc.*, 125, 1407-1425.

797 Schraff, C., H. Reich, A. Rhodin, A. Schomburg, K. Stephan, A. Perianez, and R. Potthast, 2016:
798 Kilometer-Scale ensemble data assimilation for the COSMO model (KENDA). *Q. J. R. Meteorol.*
799 *Soc.*, 142, 1453-1472.

800 Schmetz, J., P. Pili, S. Tjemkes, D. Just, J. Lerkmann, S. Rota, and A. Ratier, 2002: An intro-
801 duction to Meteosat Second Generation (MSG). *Bull. Amer. Meteor. Soc.*, 83, 977-992.

802 Seifert A, and K. Beheng, 2001: A double-moment parameterization for simulating auto-
803 conversion, accretion and selfcollection. *Atmos. Res.*, 59-60, 265-281, doi:10.1016/S0169-
804 8095(01)00126-0.

805 Stengel, M., P. Unden, M. Lindskog, P. Dahlgren, N. Gustafsson, and R. Bennartz, 2009: As-
806 similation of SEVIRI infrared radiances with HIRLAM 4D-Var. *Quart. J. Roy. Meteor. Soc.*, 135,
807 2100-2109.

808 Stengel, M., M. Lindskog, P. Unden, and N. Gustafsson, 2013: The impact of cloud-affected IR
809 radiances on forecast accuracy of a limited-area NWP model. *Quart. J. Roy. Meteor. Soc.*, 139,
810 2081-2096.

811 Szunyogh, I., E. J. Kostelich, G. Gyarmati, E. Kalnay, and B. R. Hunt, 2008: A local ensemble
812 transform Kalman filter data assimilation system for the NCEP global model. *Tellus* 60A, 113-
813 130.

814 Tavolato, C., and L. Isaksen, 2015: On the use of a Huber norm for observation quality control
815 in the ECMWF 4D-Var. *J. Roy. Meteor. Soc.*, 141, 1514-1527.

816 Thompson, G., M. Tewari, K. Ikeda, S. Tessendorf, C. Weeks, J. A. Otkin, and F. Kong, 2016:
817 Explicitly-coupled cloud physics and radiation parameterizations and subsequent evaluation in
818 WRF high-resolution convective forecasts. *Atmos. Res.*, 168, 92-104.

819 Tiedtke M., 1989: A comprehensive mass flux scheme for cumulus parameterisation in large-
820 scale models. *Mon. Wea. Rev.* 117, 1779-1799.

821 Vukicevic, T., M. Sengupta, A. S. Jones, and T. Vonder Haar, 2006: Cloud-resolving satellite
822 data assimilation: Information content of IR window observations and uncertainties in estimation.
823 *J. Atmos. Sci.*, 63, 901-919.

824 Wyser K. 1998: The effective radius in ice clouds. *J. Climate* 11, 7, 1793-1802.

825 Yang, P., L. Bi, B. A. Baum, K.-N. Liou, G. Kattawar, M. Mishchenko, and B. Cole, 2013:
826 Spectrally consistent scattering, absorption, and polarization properties of atmospheric ice crystals
827 at wavelengths from 0.2 μ m to 100 μ m. *J. Atmos. Sci.*, 70, 330-347.

828 Zangl G., D. Reinert, P. Ripodas, and M. Baldauf, 2015: The ICON (ICOsahedral Non-
829 hydrostatic) modelling framework of DWD and MPI-M: Description of the non-hydrostatic dy-
830 namical core. *Q. J. R. Meteorol. Soc.*, 141, 563-579, doi:10.1002/qj.2378.

831 Zhang F., C. Snyder, and J. Sun, 2004: Impacts of initial estimate and observation availability
832 on convective-scale data assimilation with an ensemble Kalman filter. *Mon. Wea. Rev.*, 132,
833 1238-1253.

834 Zhu Y., J. Derber, A. Collard, D. Dee, R. Treadon, G. Gayno, and J. A. Jung, 2014: En-
835 hanced radiance bias correction in the National Centers for Environmental Prediction's Grid-
836 point Statistical Interpolation data assimilation system. *Q. J. R. Meteorol. Soc.*, 140, 1479-1492,
837 doi:10.1002/qj.2233.

838 Zhu, Y., J. C. Derber, R. J. Purser, B. A. Ballish, and J. Whiting, 2015: Variational correction of
839 aircraft temperature bias in the NCEP's GSI analysis system. *Mon. Wea. Rev.*, 143, 3774-3803.

840 Zhu, Y., and CoAuthors, 2016: All-sky microwave radiance assimilation in NCEP's GSI analysis
841 system. *Mon. Wea. Rev.*, 144, 4709-4735.

842 **7. Figure Captions**

843 Fig. 1. Observed SEVIRI 6.2 μm brightness temperatures (K) valid at 18 UTC on (a) 16 May,
844 (b) 17 May, (c) 18 May, (d) 19 May, and (e) 20 May 2014.

845 Fig. 2. Probability distributions of 6.2 μm observation-minus-background departures plotted
846 as a function of the observed 6.2 μm brightness temperatures (K) for the (a) original data, and
847 the (b) constant, (c) 1st order, (d) 2nd order, and (e) 3rd order bias corrected observations when
848 the observed 6.2 μm brightness temperature is used as the predictor. The horizontal black line
849 segments represent the conditional bias in each column. Data were accumulated at hourly intervals
850 during a 108-h period from 13 UTC on 16 May 2014 to 00 UTC on 20 May 2014.

851 Fig. 3. Probability density function of normalized 6.2 μm observation-minus-background de-
852 partures for the (a) original and (b) constant bias correction distributions. The corresponding 1st,
853 2nd, and 3rd order bias correction error distributions when the (c-e) observed 6.2 μm brightness

854 temperatures, (f-h), NWC SAF cloud top heights, (i-k) model-simulated total integrated water
855 content (IWC) in the 100-700 hPa layer, (l-n) satellite zenith angle, or (o-q) observed $6.2 \mu\text{m}$
856 brightness temperatures, satellite zenith angle, and IWC are used as the predictors are also shown.
857 Data were accumulated at hourly intervals during a 108-h period from 13 UTC on 16 May 2014
858 to 00 UTC on 20 May 2014.

859 Fig. 4. Same as Fig. 2 except for showing probability distributions plotted as a function of the
860 NWC SAF cloud top height retrieval (km) when this quantity is also used as the BC predictor.

861 Fig. 5. Same as Fig. 2 except for showing probability distributions plotted as a function of the
862 vertically-integrated total water content (mm) over the 100-700 hPa layer when this quantity is
863 also used as the BC predictor.

864 Fig. 6. Same as Fig. 2 except for showing probability distributions plotted as a function of the
865 satellite zenith angle (θ) when this quantity is also used as the BC predictor.

866 Fig. 7. Same as Fig. 2 except for showing probability distributions for clear-sky matched
867 observations plotted as a function of the observed brightness temperature (K) when this quantity
868 is also used as the BC predictor.

869 Fig. 8. Probability density function of normalized clear-sky matched $6.2 \mu\text{m}$ observation-
870 minus-background departures for the (a) original data, and the (b) constant, (c) 1st order, (d)
871 2nd order, and (e) 3rd order bias corrected observations when the observed $6.2 \mu\text{m}$ brightness
872 temperature is used as the predictor. Data were accumulated at hourly intervals during a 108-h
873 period from 13 UTC on 16 May 2014 to 00 UTC on 20 May 2014.

874 Fig. 9. Same as Fig. 2 except for showing probability distributions for cloudy-sky matched
875 observations plotted as a function of the NWC SAF cloud top height retrieval (km) when this
876 quantity is also used as the BC predictor.

877 Fig. 10. Probability density function of normalized cloudy-sky matched $6.2 \mu\text{m}$ observation-
878 minus-background departures for the (a) original data, and the (b) constant, (c) 1st order, (d) 2nd
879 order, and (e) 3rd order bias corrected observations when the NWC SAF cloud top height retrieval
880 is used as the predictor. Data were accumulated at hourly intervals during a 108-h period from 13
881 UTC on 16 May 2014 to 00 UTC on 20 May 2014.

882 Fig. 11. Same as Fig. 2 except for showing probability distributions plotted as a function of
883 the observed $6.2 \mu\text{m}$ brightness temperatures when the observed $6.2 \mu\text{m}$ brightness temperature,
884 satellite zenith angle, and vertically-integrated total water content from 100-700 hPa are used as
885 the BC predictors.

886 Fig. 12. Probability distributions of $7.3 \mu\text{m}$ observation-minus-background departures plotted
887 as a function of the observed $7.3 \mu\text{m}$ brightness temperatures (K) for the (a) original data, and the
888 (b) constant, (c) 1st order, (d) 2nd order, and (e) 3rd order bias corrected observations when the
889 observed $7.3 \mu\text{m}$ brightness temperature, satellite zenith angle, and model-integrated total water
890 content from 100-700 hPa are used as the predictors. Data were accumulated at hourly intervals
891 during a 108-h period from 13 UTC on 16 May 2014 to 00 UTC on 20 May 2014.

892 Fig. 13. Probability density function of normalized $7.3 \mu\text{m}$ observation-minus-background
893 departures for the (a) original data, and the (b) constant, (c) 1st order, (d) 2nd order, and (e) 3rd
894 order bias corrected observations when the observed $7.3 \mu\text{m}$ brightness temperatures are used as
895 the predictor. Data were accumulated at hourly intervals during a 108-h period from 13 UTC on
896 16 May 2014 to 00 UTC on 20 May 2014.

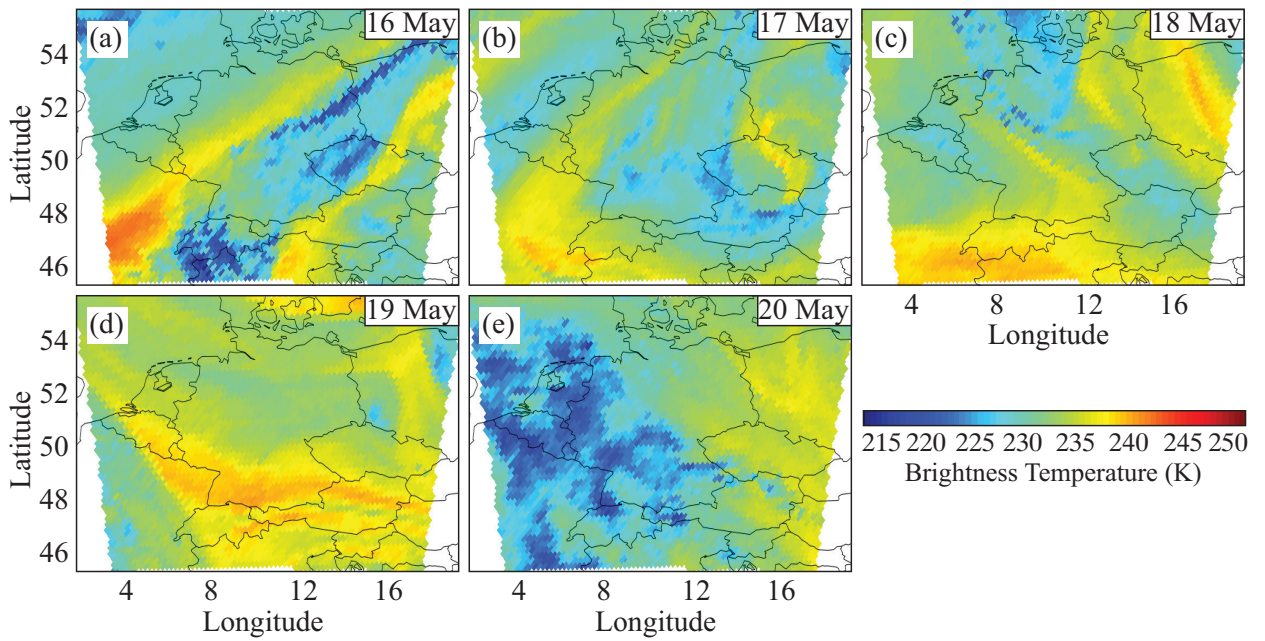


Fig. 1. Observed SEVIRI 6.2 μm brightness temperatures (K) valid at 18 UTC on (a) 16 May, (b) 17 May, (c) 18 May, (d) 19 May, and (e) 20 May 2014.

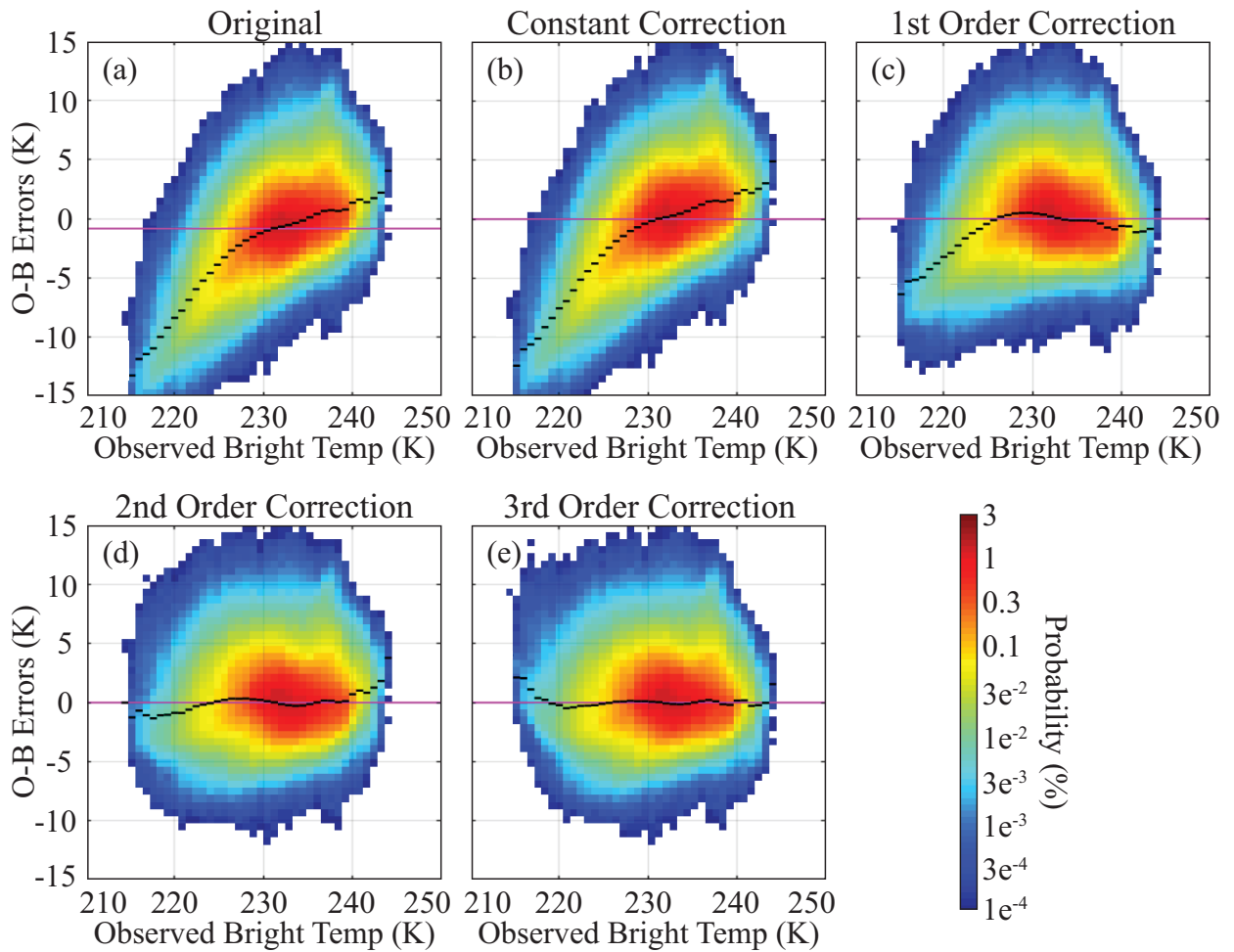


Fig. 2. Probability distributions of 6.2 μm observation-minus-background departures plotted as a function of the observed 6.2 μm brightness temperatures (K) for the (a) original data, and the (b) constant, (c) 1st order, (d) 2nd order, and (e) 3rd order bias corrected observations when the observed 6.2 μm brightness temperature is used as the predictor. The horizontal black line segments represent the conditional bias in each column. Data were accumulated at hourly intervals during a 108-h period from 13 UTC on 16 May 2014 to 00 UTC on 20 May 2014.

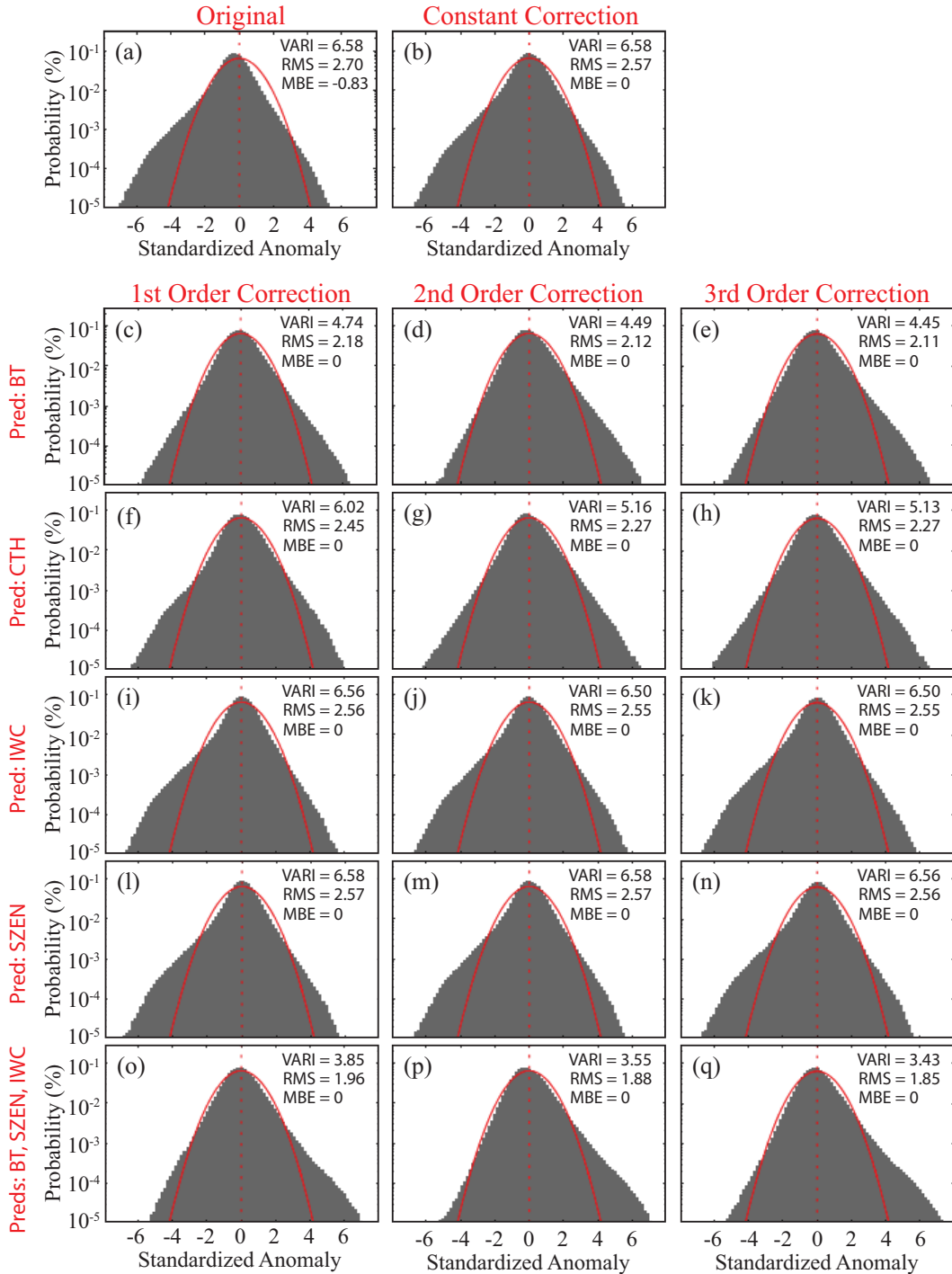


Fig. 3. Probability density function of normalized $6.2 \mu\text{m}$ observation-minus-background departures for the (a) original and (b) constant bias correction distributions. The corresponding 1st, 2nd, and 3rd order bias correction error distributions when the (c-e) observed $6.2 \mu\text{m}$ brightness temperatures, (f-h) NWC SAF cloud top heights, (i-k) model-simulated total integrated water content (IWC) in the 100-700 hPa layer, (l-n) satellite zenith angle, or (o-q) observed $6.2 \mu\text{m}$ brightness temperatures, satellite zenith angle, and IWC are used as the predictors are also shown. Data were accumulated at hourly intervals during a 108-h period from 13 UTC on 16 May 2014 to 00 UTC on 20 May 2014.

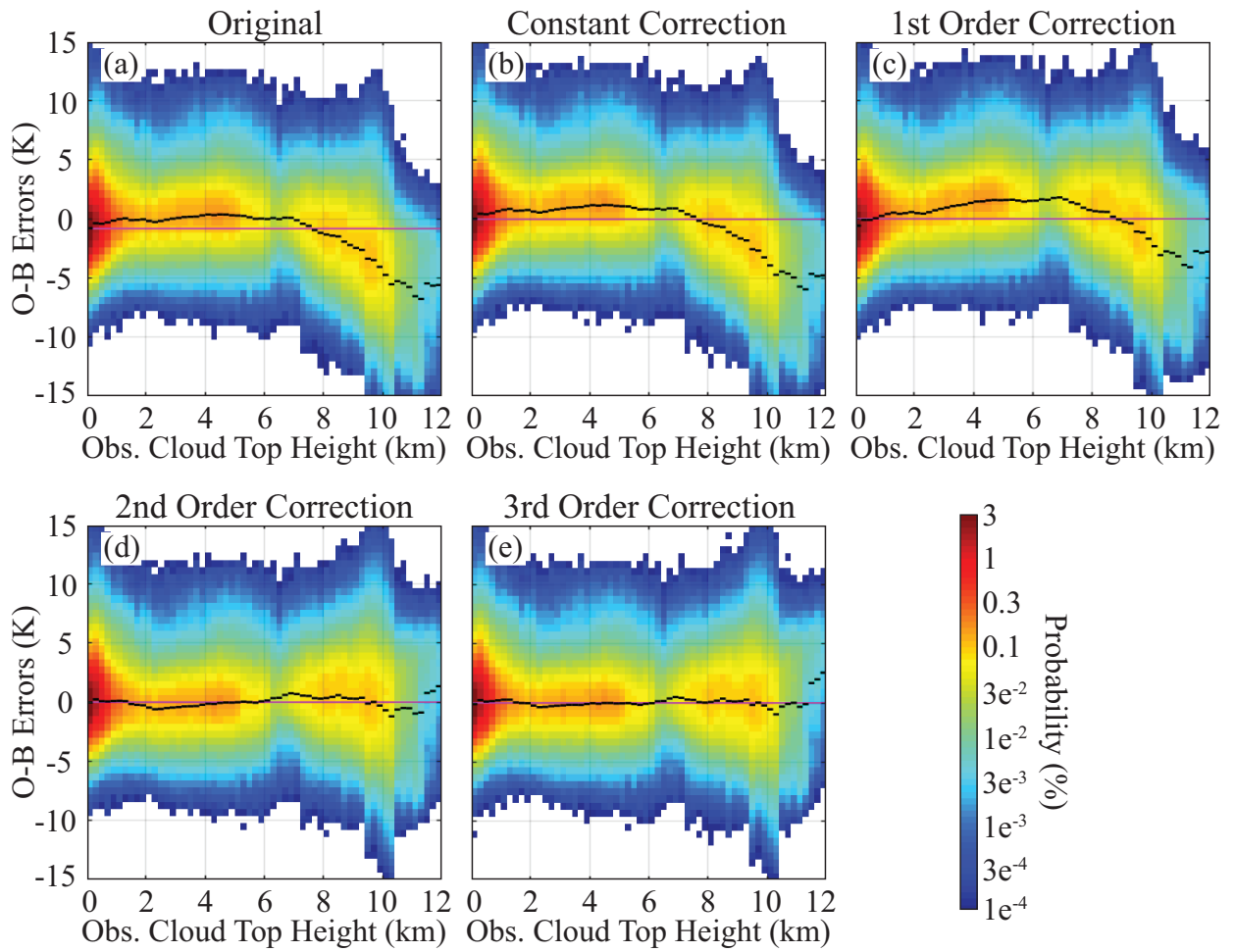


Fig. 4. Same as Fig. 2 except for showing probability distributions plotted as a function of the NWC SAF cloud top height retrieval (km) when this quantity is also used as the BC predictor.

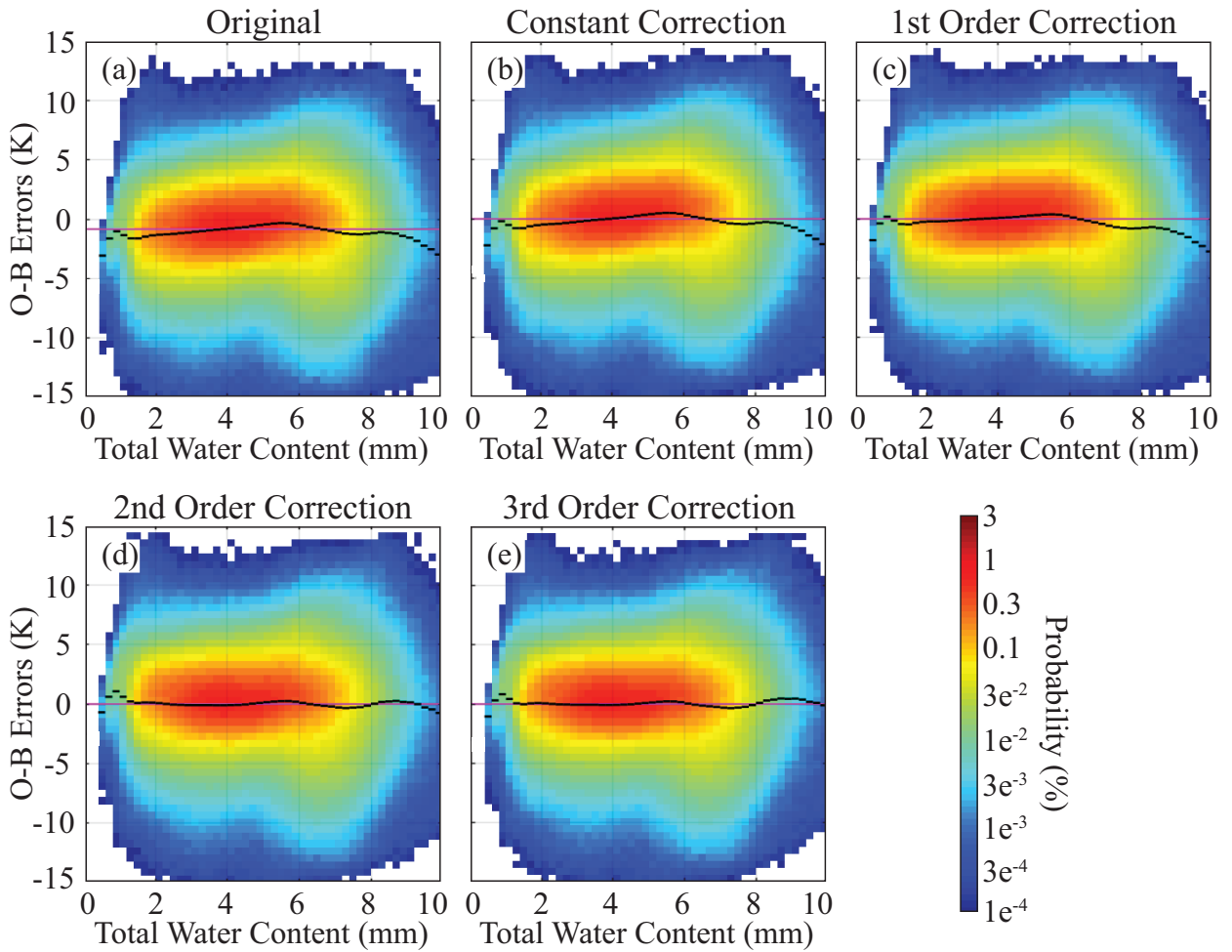


Fig. 5. Same as Fig. 2 except for showing probability distributions plotted as a function of the vertically-integrated total water content (mm) over the 100-700 hPa layer when this quantity is also used as the BC predictor.

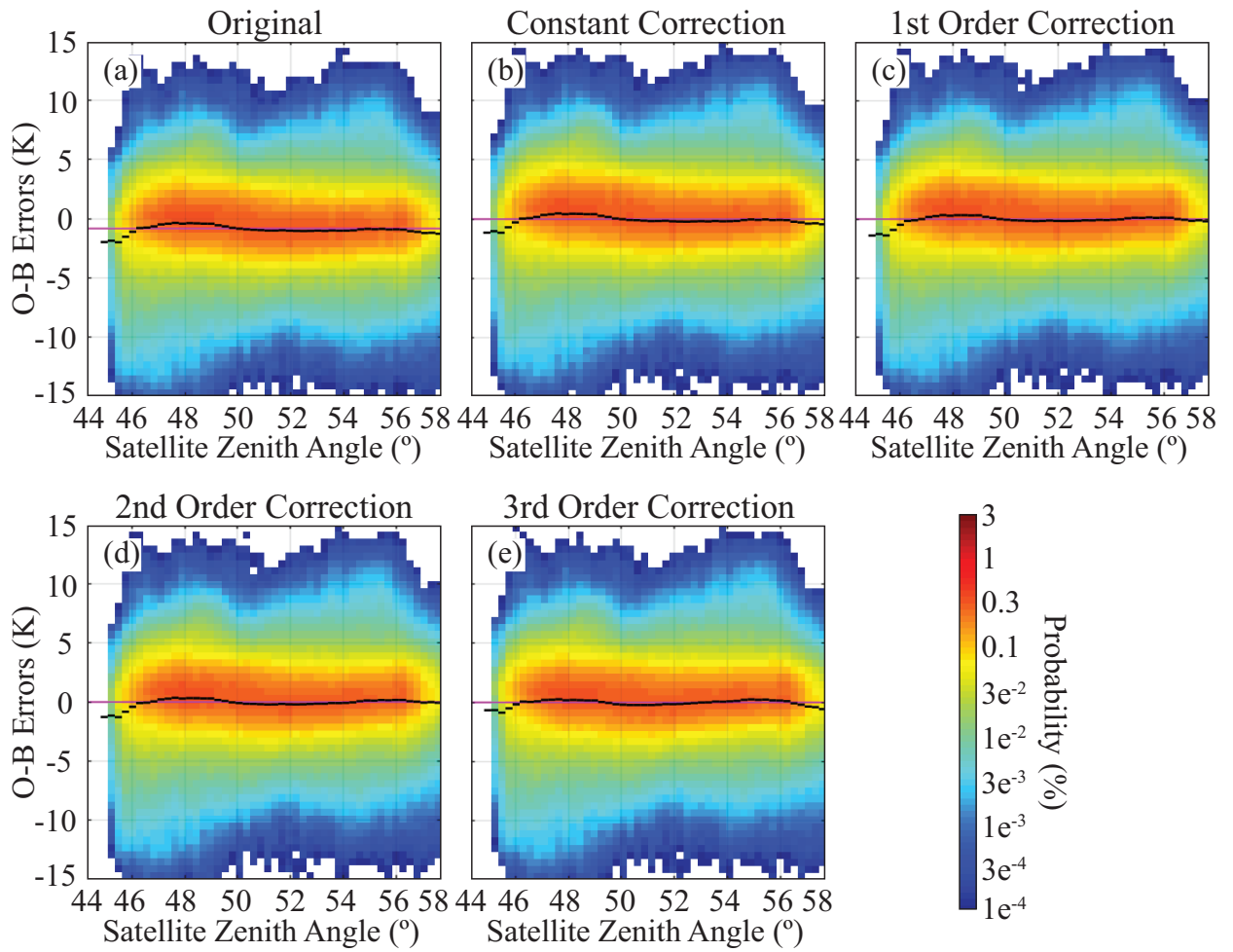


Fig. 6. Same as Fig. 2 except for showing probability distributions plotted as a function of the satellite zenith angle ($^{\circ}$) when this quantity is also used as the BC predictor.

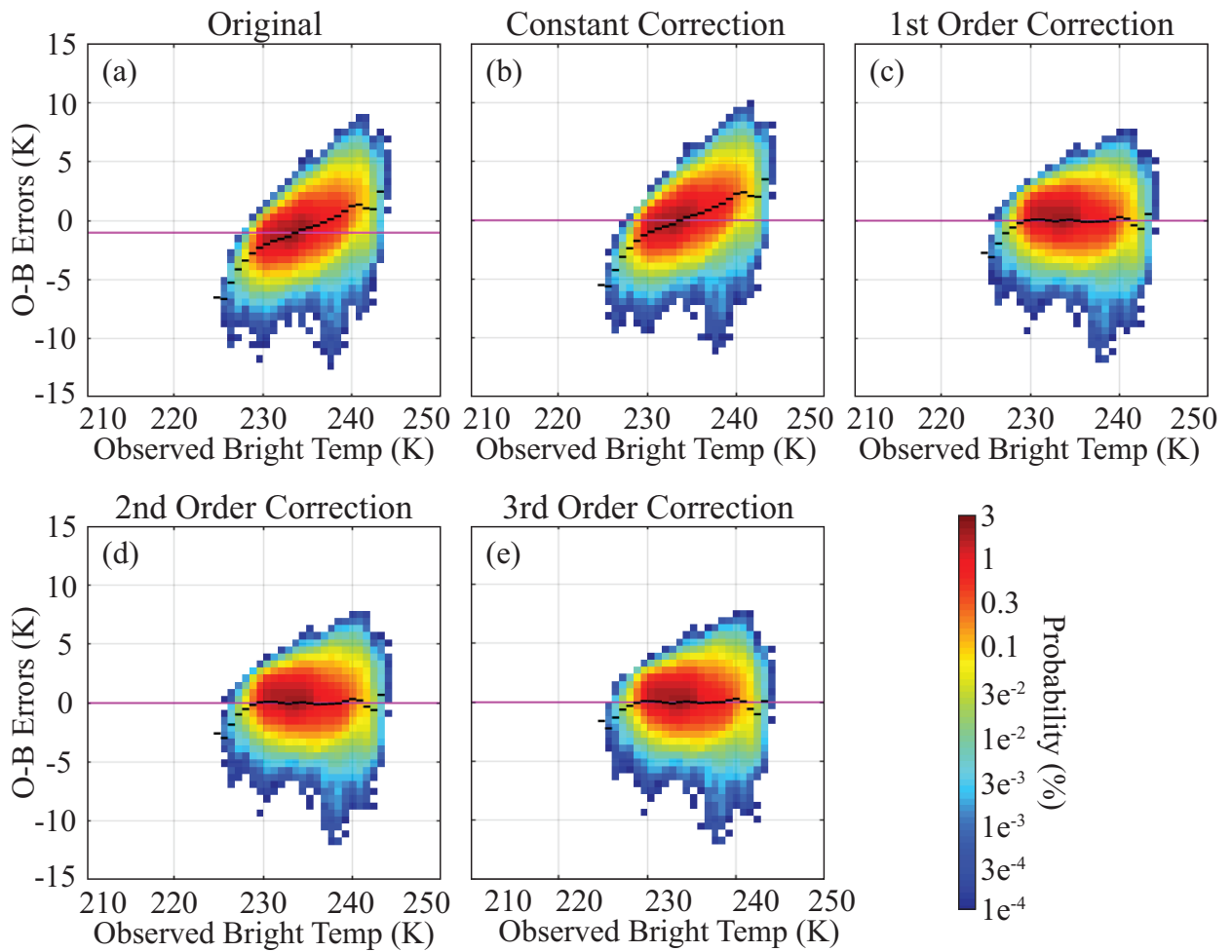


Fig. 7. Same as Fig. 2 except for showing probability distributions for clear-sky matched observations plotted as a function of the observed brightness temperature (K) when this quantity is also used as the BC predictor.

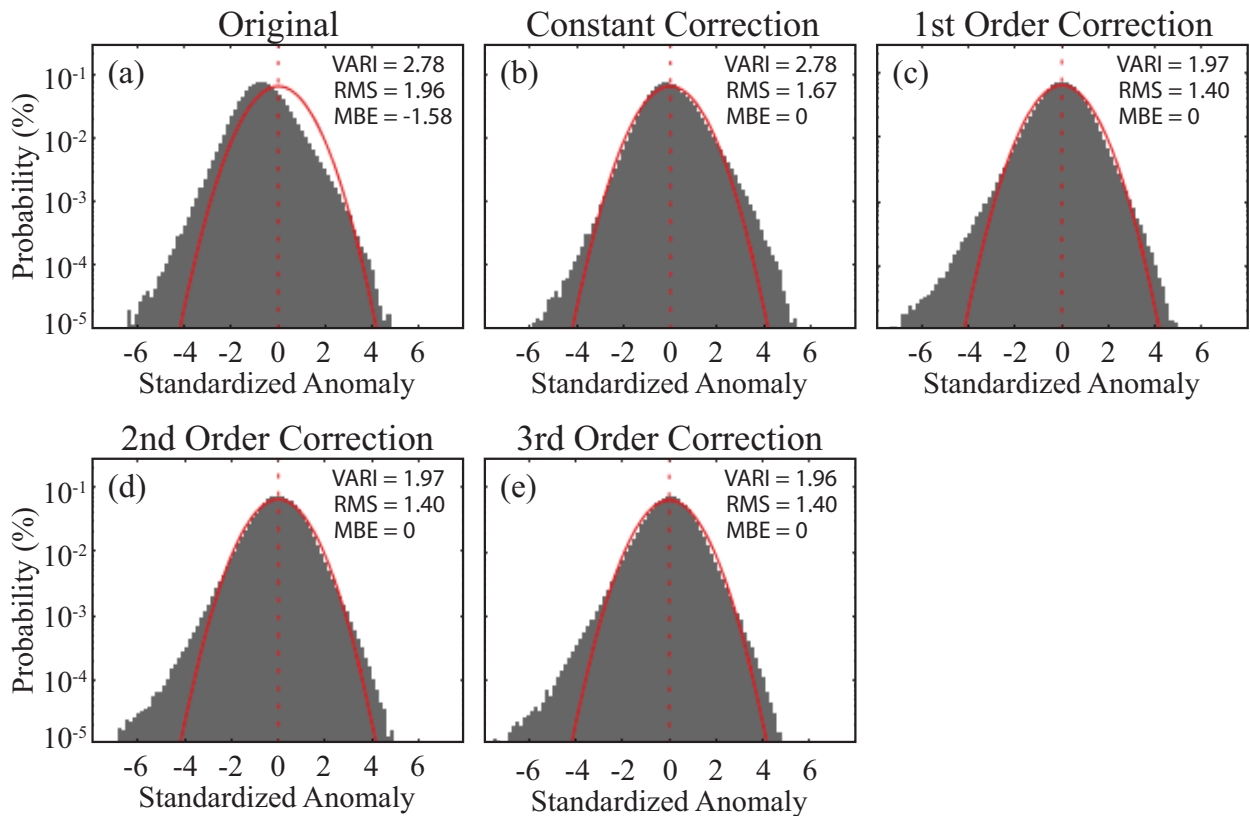


Fig. 8. Probability density function of normalized clear-sky matched $6.2 \mu\text{m}$ observation-minus-background departures for the (a) original data, and the (b) constant, (c) 1st order, (d) 2nd order, and (e) 3rd order bias corrected observations when the observed $6.2 \mu\text{m}$ brightness temperature is used as the predictor. Data were accumulated at hourly intervals during a 108-h period from 13 UTC on 16 May 2014 to 00 UTC on 20 May 2014.

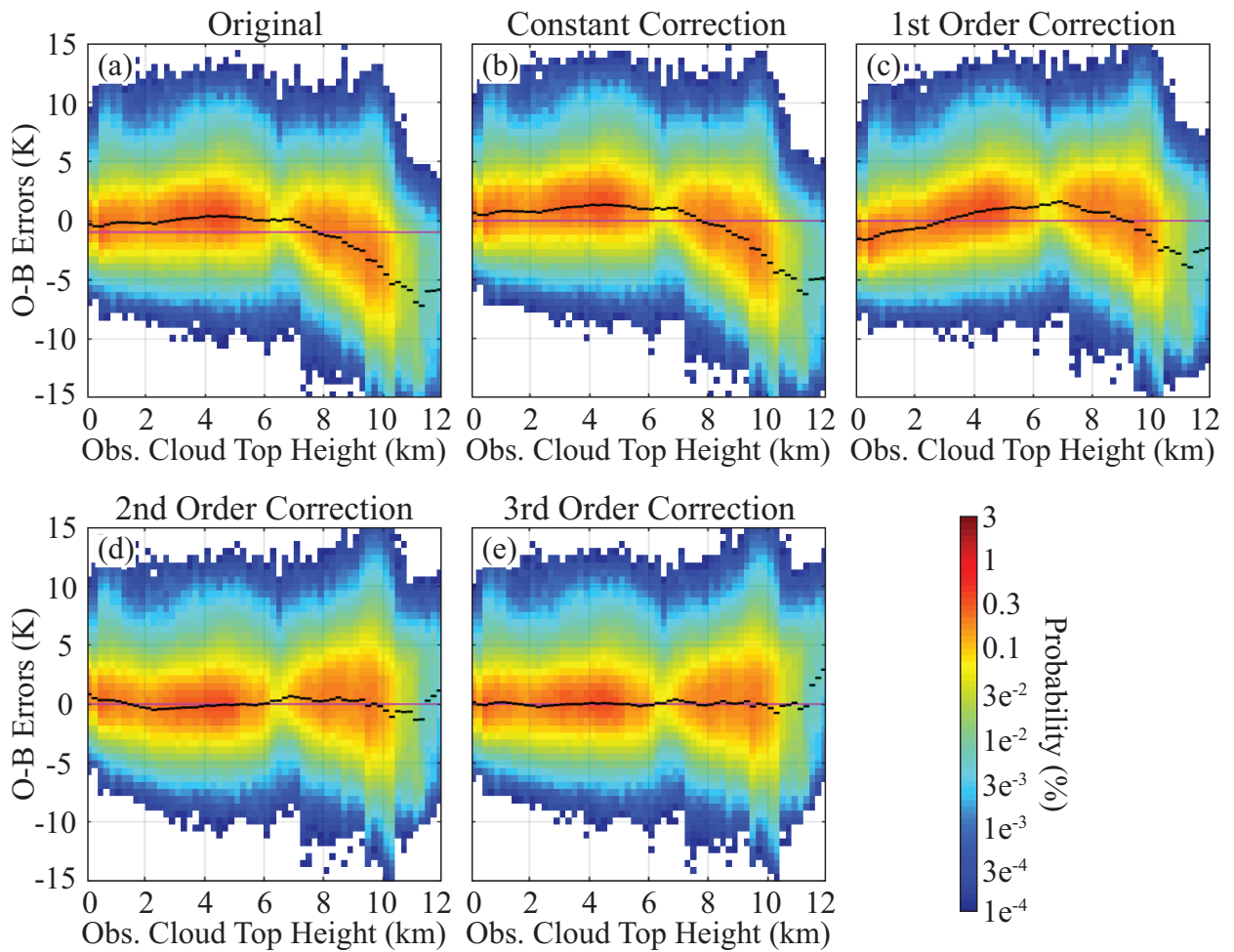


Fig. 9. Same as Fig. 2 except for showing probability distributions for cloudy-sky matched observations plotted as a function of the NWC SAF cloud top height retrieval (km) when this quantity is also used as the BC predictor.

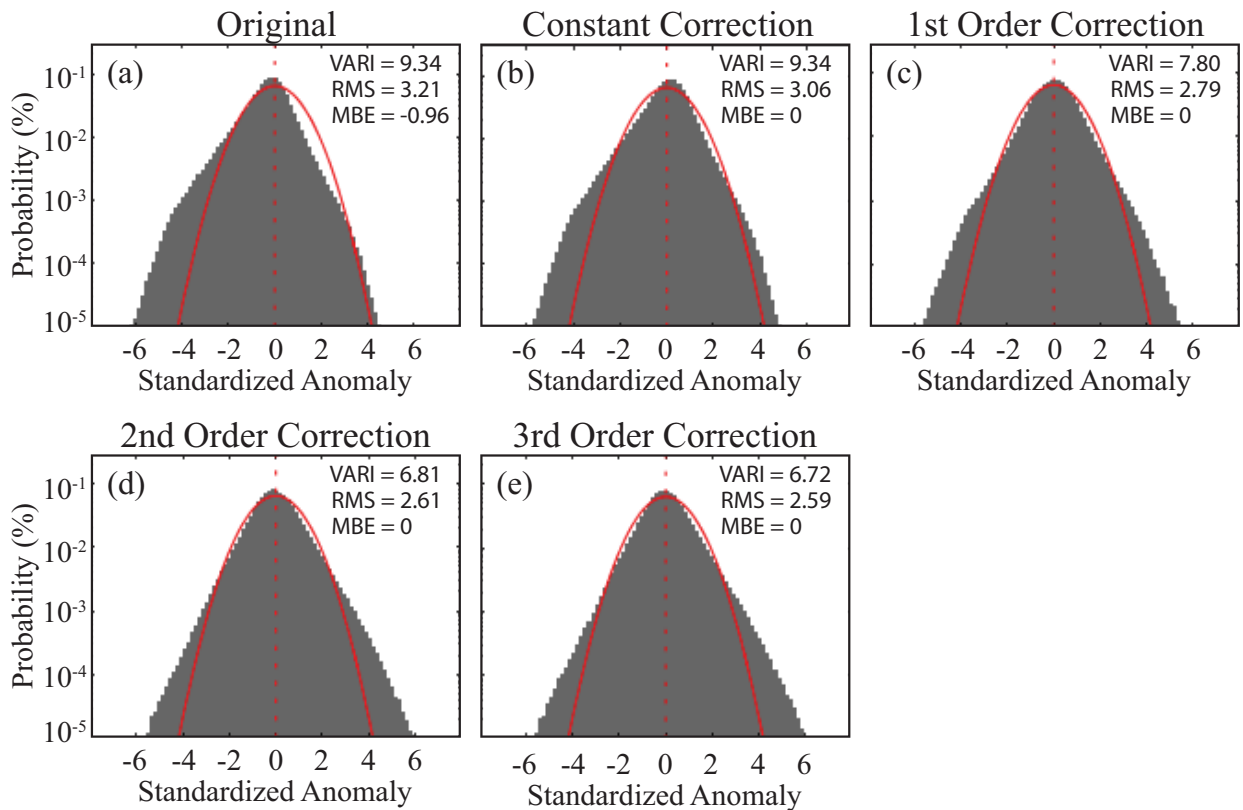


Fig. 10. Probability density function of normalized cloudy-sky matched $6.2 \mu\text{m}$ observation-minus-background departures for the (a) original data, and the (b) constant, (c) 1st order, (d) 2nd order, and (e) 3rd order bias corrected observations when the NWC SAF cloud top height retrieval is used as the predictor. Data were accumulated at hourly intervals during a 108-h period from 13 UTC on 16 May 2014 to 00 UTC on 20 May 2014.

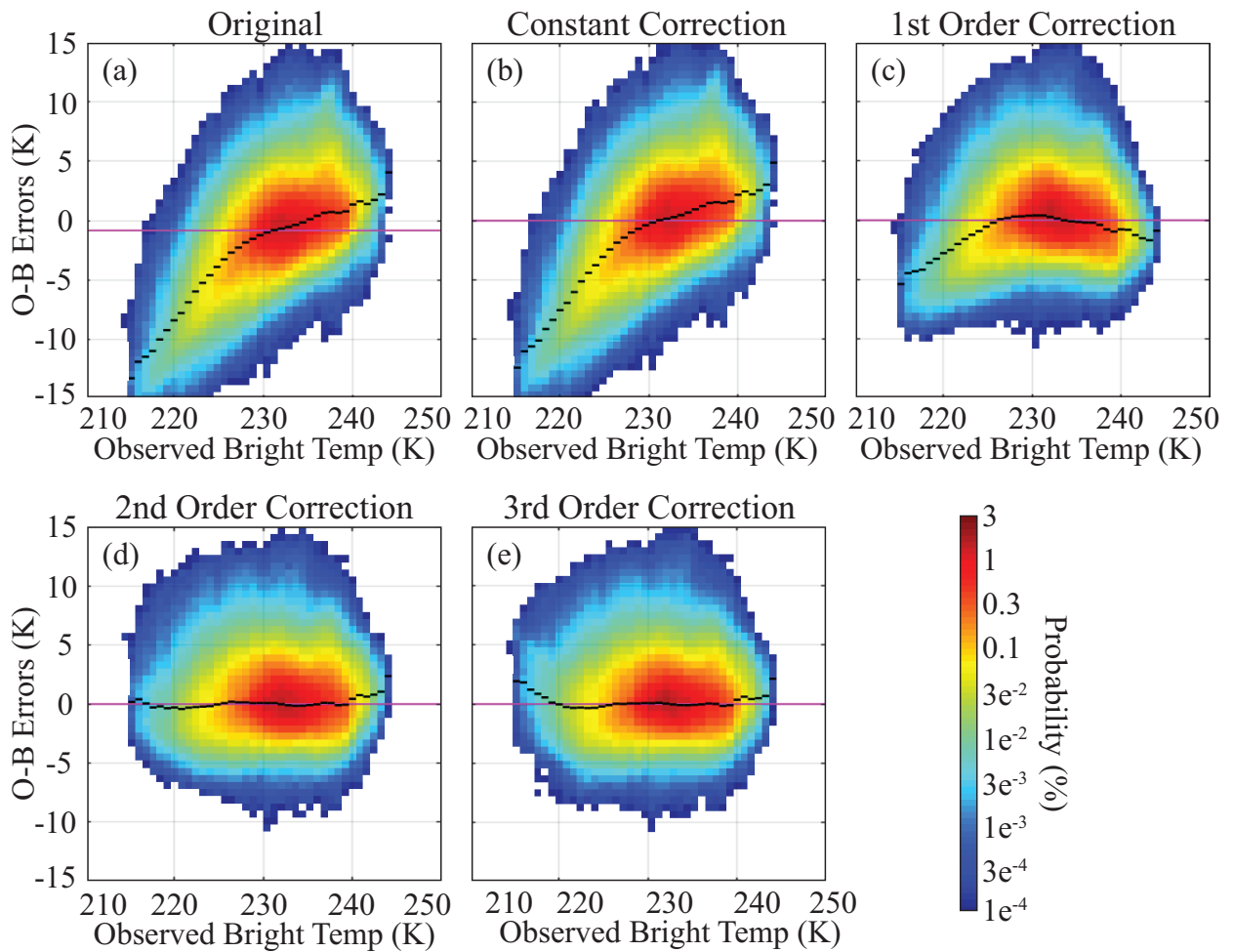


Fig. 11. Same as Fig. 2 except for showing probability distributions plotted as a function of the observed $6.2 \mu\text{m}$ brightness temperatures when the observed $6.2 \mu\text{m}$ brightness temperature, satellite zenith angle, and vertically-integrated total water content from 100-700 hPa are used as the BC predictors.

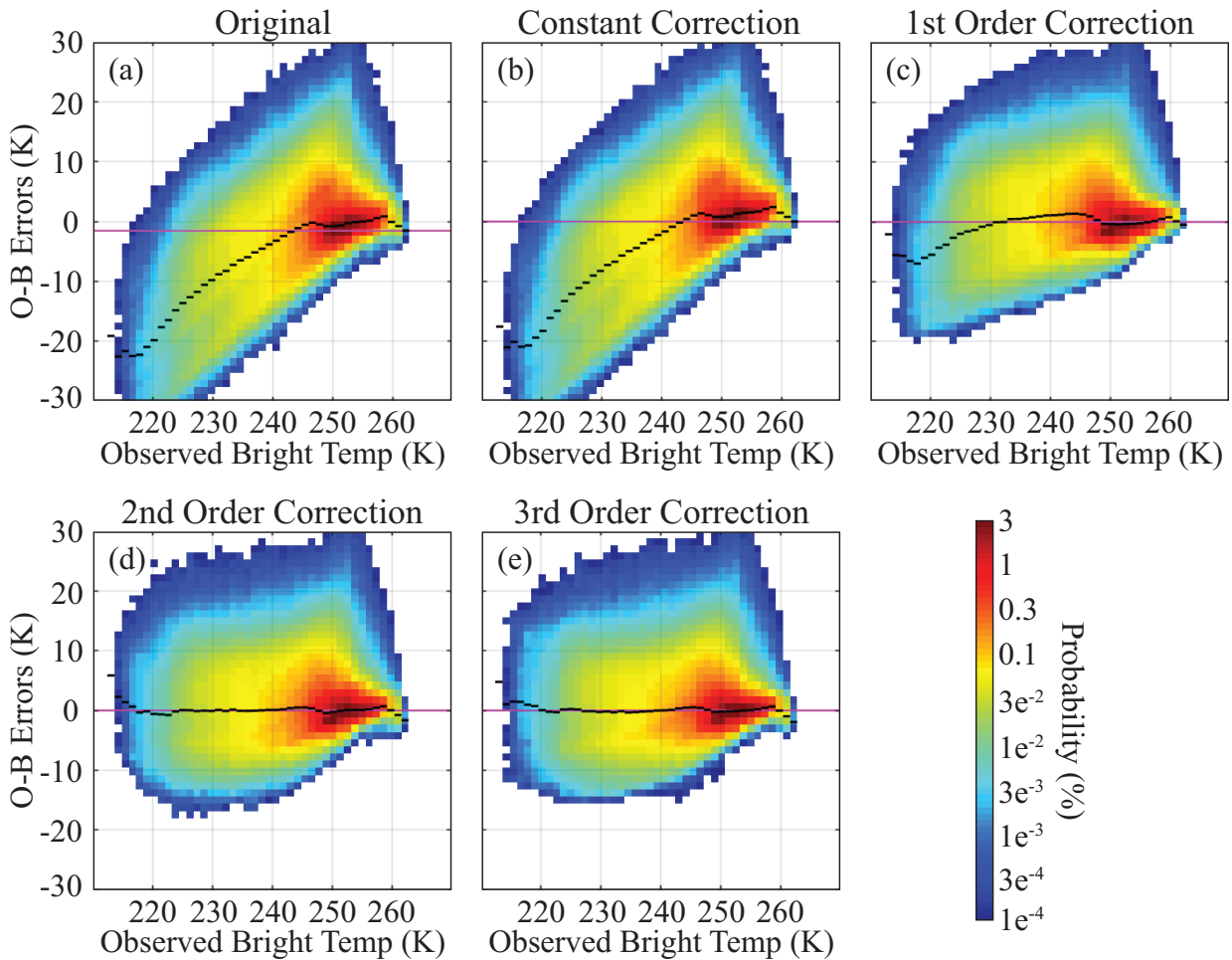


Fig. 12. Probability distributions of 7.3 μm observation-minus-background departures plotted as a function of the observed 7.3 μm brightness temperatures (K) for the (a) original data, and the (b) constant, (c) 1st order, (d) 2nd order, and (e) 3rd order bias corrected observations when the observed 7.3 μm brightness temperature, satellite zenith angle, and model-integrated total water content from 100-700 hPa are used as the predictors. Data were accumulated at hourly intervals during a 108-h period from 13 UTC on 16 May 2014 to 00 UTC on 20 May 2014.

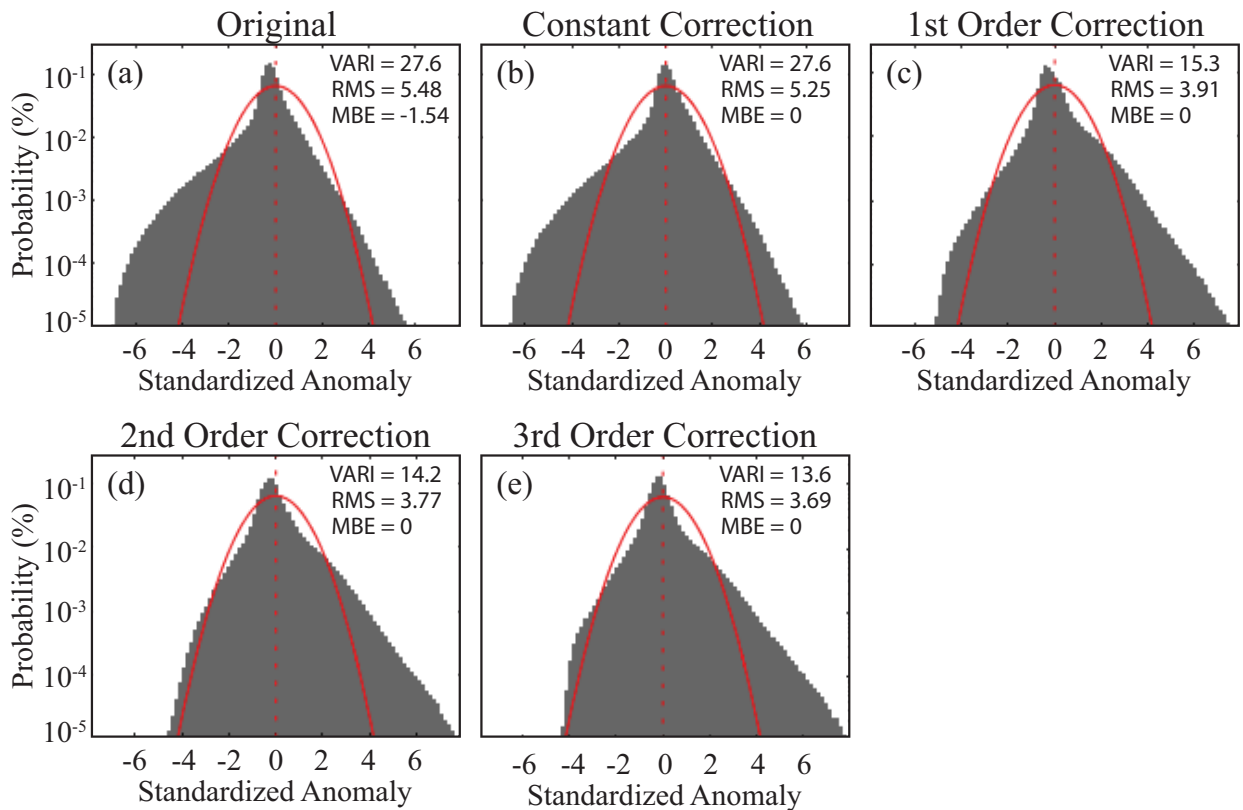


Fig. 13. Probability density function of normalized $7.3 \mu\text{m}$ observation-minus-background departures for the (a) original data, and the (b) constant, (c) 1st order, (d) 2nd order, and (e) 3rd order bias corrected observations when the observed $7.3 \mu\text{m}$ brightness temperatures are used as the predictor. Data were accumulated at hourly intervals during a 108-h period from 13 UTC on 16 May 2014 to 00 UTC on 20 May 2014.